



Open Research Online

The Open University's repository of research publications and other research outputs

Venus: A phase equilibria approach to model surface alteration as a function of rock composition, oxygen- and sulfur fugacities

Journal Item

How to cite:

Semprich, Julia; Filiberto, Justin and Treiman, Allan H. (2020). Venus: A phase equilibria approach to model surface alteration as a function of rock composition, oxygen- and sulfur fugacities. *Icarus*, 346, article no. 113779.

For guidance on citations see [FAQs](#).

© 2020 Elsevier Inc.



<https://creativecommons.org/licenses/by-nc-nd/4.0/>

Version: Accepted Manuscript

Link(s) to article on publisher's website:

<http://dx.doi.org/doi:10.1016/j.icarus.2020.113779>

Copyright and Moral Rights for the articles on this site are retained by the individual authors and/or other copyright owners. For more information on Open Research Online's data [policy](#) on reuse of materials please consult the policies page.

oro.open.ac.uk

1 **Venus: A phase equilibria approach to model surface alteration as a**
2 **function of rock composition, oxygen- and sulfur fugacities**

3 Julia Semprich^{1,2}, Justin Filiberto¹, and Allan H. Treiman¹

4 ¹Lunar and Planetary Institute, USRA, 3600 Bay Area Blvd. Houston TX 77058, USA

5 ²AstrobiologyOU, School of Environment, Earth & Ecosystem Sciences, Walton Hall, Milton
6 Keynes, MK7 6AA, UK

7 Corresponding author: julia.semprich@open.ac.uk

8
9
10 **Abstract**

11 Rock alteration processes on Venus are still poorly understood due to the limited geochemical
12 data on surface rocks and uncertainties in atmospheric compositions. We use phase equilibria
13 calculations to constrain mineral stabilities at Venus surface conditions for different rock and gas
14 compositions resulting in the chemical system SiO₂-TiO₂-Al₂O₃-FeO-MgO-CaO-Na₂O-K₂O with C-
15 O-H-S gas at varying O₂ and S₂ fugacities. While the low concentrations of H₂O in the present-
16 day atmosphere result in conditions, under which anhydrous mineral assemblages dominate,
17 higher amounts of water, possibly during an earlier stage in Venus' history, could have resulted
18 in the formation of amphibole and biotite. Even in a sulfur-free atmosphere, carbonates would be
19 stable only in alkali-rich basalts. The presence of SO₂ in the atmosphere, however, causes the
20 formation of anhydrite. The stabilities of iron oxides and sulfides are highly sensitive to gas
21 fugacities (i.e., the composition of the atmosphere), as well as temperature. While the modeled
22 magnetite-hematite transition is located close to conditions relevant for planetary radius, the
23 assemblage of anhydrite + hematite ± pyrite may be stable at higher elevations if a similar range
24 of f_{O_2} as at the lowlands is assumed. Therefore, our model agrees with pyrite proposed as cause
25 of the high radar backscatter observed at high elevations in the northern highlands.

26 **Keywords:** Venus, surface; Rock alteration; Phase equilibria modeling; Iron oxides and sulfides

27 **1. Introduction**

28 Our knowledge of Venus' surface geochemistry and petrology is still limited due to the dense
29 atmosphere and high surface temperature impeding remote sensing and *in situ* measurements of
30 rock compositions. The most detailed geochemical constraints were obtained by the incomplete
31 major and radioactive (U, Th, K) element data from the Venera and VEGA landers (Surkov et al.,
32 1984, 1986), and isotopic ratios of noble gases in the lower atmosphere (von Zahn et al., 1983;
33 Esposito et al., 1997). Further evidence for the composition of surface rocks comes from radar
34 imaging (e.g., Masursky et al., 1980; Ivanov and Head, 2011; Tanaka et al., 1997) and near-
35 infrared radiance measurements through atmospheric spectral windows near 1 μm , providing
36 information that can be related to surface mineralogy and the compositional variation of surface
37 features (e.g., Hashimoto et al., 2008; Gilmore et al., 2017). Studying rock alteration in contact
38 with the atmosphere is hence limited to the experimental investigations of reactions in analog
39 rocks and thermodynamic modeling. In this contribution, we use phase equilibria calculations to
40 model phase relations of likely venusian whole-rock compositions in contact with the atmosphere
41 at a range of conditions relevant for both modal planetary radius and higher elevations.

42 Radar imaging and altimetry measurements of Venus' surface area reveal a geologically
43 complex surface comprising plains, volcanic/tectonic rises, and elevated areas composed of
44 tectonically deformed tesserae (Ivanov and Head, 2011; Tanaka et al., 1997). Volcanic plains are
45 the dominant landform, ~60-70% of the planet. Morphological features inferred from Magellan
46 radar imaging (Head et al., 1992; Weitz and Basilevsky, 1993; Campbell et al., 1997; Ivanov and
47 Head, 2011), combined with the partial *in situ* chemical analyses of Venus surface materials by
48 Venera and VEGA landers (Surkov et al., 1984, 1986), suggest that the volcanic plains and rises
49 are composed of basaltic rocks. Analyzed rock compositions are broadly similar to olivine
50 tholeiites from Earth's mid-ocean ridges and alkali basalts from Earth's ocean islands (Basilevsky

51 et al., 1992; Kargel et al., 1993; Grimm and Hess, 1997; Fegley, 2014; Treiman, 2007; Filiberto,
52 2014).

53 In contrast, tesserae terrain covers only ~8% of the surface of Venus and consistently
54 appears as the stratigraphically oldest material (e.g. Ivanov and Head, 1996). In the absence of
55 *in situ* measurements and direct morphological evidence, the composition of tessera terrains
56 remain unknown. Some constraint is provided by measurements of near-infrared surface
57 emission of some tesserae showing values that are distinctly lower than those of the surrounding
58 basaltic plains (Hashimoto et al., 2008; Helbert et al., 2008; Mueller et al., 2008; Basilevsky et al.,
59 2012; Gilmore et al., 2015). This difference has been interpreted to mean that the tesserae have
60 more felsic and less iron-rich compositions, like granitic rock (e.g. Hashimoto et al., 2008; Gilmore
61 et al., 2015). However, 1 μm emissivity can be affected by other factors, such as grain size,
62 surface roughness, porosity, and presence of low-emissivity weathering products that form only
63 at higher elevations (e.g. Gilmore et al., 2017). The presence of felsic igneous rocks would either
64 imply partial melting of hydrous materials resulting from recycled surface fluids into the Venus
65 interior, assuming that Venus had higher water content and putative oceans early in its history
66 (Donahue et al., 1982; Kasting and Pollack, 1983; Kumar and Taylor, 1985a; Bergh et al., 1991;
67 Krasnopolsky, 2010; Way et al., 2016), or differentiation of basaltic melts (Hashimoto et al., 2008;
68 Shellnutt, 2013, 2018; Filiberto, 2014).

69 Beyond these hints of unusual bulk composition, tesserae in northern latitudes such as
70 Maxwell Montes and other mountain ranges around Ishtar Terra show an abrupt change in radar
71 backscatter – above ~5 km elevation, they have very high backscatter (high reflectivity) and
72 appear in SAR images as if they were covered with ‘snow’ (Masursky et al., 1980; Pettengill et
73 al., 1988; Garvin et al., 1985; Klose et al., 1992; Pettengill et al., 1992; Simpson et al., 2009;
74 Treiman et al., 2016). The cause and nature of this ‘snow,’ and the abrupt change in radar
75 backscatter at a ‘snow line’ in the northern highlands have been debated vigorously. There is no

76 disagreement that the change is related to elevation, to either the decreasing pressure or
77 temperature of the atmosphere with increasing elevation (Seiff et al., 1985). One of the first
78 materials suggested was the semiconductor mineral pyrite (FeS_2) as a weathering product of
79 basalts (Ford and Pettengill, 1983; Klose et al., 1992; Pettengill et al., 1996, 1992; Wood, 1997),
80 although relatively large proportions of the mineral would be required to match the observed high
81 radar reflectivity (Gilmore et al., 2017). At lower elevations and higher temperatures, a weathering
82 product with different properties, like magnetite, is expected to be more stable and the transition
83 from magnetite to pyrite would lead to a sharp transition in radar backscatter (a “snow line”).
84 However, other works excluded the presence of pyrite based on thermochemical constraints
85 (Fegley and Treiman, 1992; Fegley et al., 1995b; Fegley, 1997). A number of other semiconductor
86 substances have been suggested as alternatives to pyrite including: metal halides and
87 chalcogenides (Brackett et al., 1995); and “heavy metal frosts” (Pettengill et al., 1996; Schaefer
88 and Fegley, 2004). Many of the suggested substances are either not stable at highlands surface
89 conditions or stable at both highlands and lowlands conditions (Kohler et al., 2013, 2014). Others
90 are exceptionally rare or unknown in terrestrial basaltic rocks (e.g. Gilmore et al., 2017).

91 The radar reflectivity of the northern highlands differs significantly from that observed at
92 Ovda Regio and other near-equatorial highlands, where the backscatter coefficients rise with
93 elevation to a maximum at 4.5 km and then drop precipitously (Klose et al., 1992; Arvidson et al.,
94 1994; Treiman et al., 2016). This pattern can be explained by a substance that transitions from
95 ferroelectric to dielectric such as chlorapatite (Treiman et al., 2016) or anhydrous calcium
96 phosphates (Lazoryak et al., 2004). The absence of a semiconductor material at Ovda implies
97 that either the atmospheric chemistry or the surface materials at Maxwell and Ovda are
98 substantially different (Treiman et al., 2016).

99 Venus surface rocks have been exposed to a hot atmosphere for at least several hundred
100 million years. The atmosphere consists mainly of CO_2 with minor N_2 , and traces of noble and

101 chemically active gases (Fegley, 2014; Marcq et al., 2018). The concentrations of SO₂, CO, COS,
102 S_n and possibly other trace gases are poorly constrained in the lower 20-30 km of the atmosphere
103 and may vary with altitude and latitude (Zolotov, 2018). At the modal planetary radius, material
104 on the surface is exposed to temperatures of 740 K (~467 °C) and pressures of 95.6 bars (Seiff
105 et al., 1985). At other elevations, conditions vary between 758-658 K and 110-47 bars.
106 Thermodynamic equilibrium between near-surface gases is assumed at planetary radius
107 (Krasnopolsky and Parshev, 1981; Fegley et al., 1997b; Krasnopolsky, 2007) but has not been
108 confirmed by in situ measurements and latitudinal variations in gas concentration may occur
109 (Zolotov, 2018). The lack of chemical equilibration between the major chemically active gases at
110 higher elevations is limiting the usefulness of gas-solid type calculations of mineral stability
111 (Zolotov, 2018, 2019).

112 Data from spacecraft exploration of Venus, in particular from the Venera and VEGA
113 landers (Surkov et al., 1984, 1986), strongly suggest the chemical alteration of Venus surface
114 rocks and fines (Zolotov, 2018, 2019). The oxidation state mainly controls which iron oxide
115 minerals may be present on the surface of Venus. The ratio of CO/CO₂ in the near-surface
116 atmosphere (Zolotov, 2015, 2018) is close to the magnetite-hematite reaction (Fegley et al.,
117 1997b; Fegley, 2014; Zolotov, 1996, 2015), with magnetite being stable at lower oxidation state
118 and hematite at higher. Maghemite, a common metastable oxidation product of magnetite, may
119 also be present as a product of surface-atmosphere alteration (Gilmore et al., 2017). Reflectance
120 spectra in visible light wavelengths suggest the presence of hematite at Venera 9 and 10 landing
121 sites while the reflectance at the Venera 13 and 14 sites was more consistent with unaltered
122 basalt (Pieters et al., 1986; Yamanoi et al., 2009). Venus basalts may therefore have weathered
123 to different degrees or different alteration products. Trapping of atmospheric S in secondary
124 minerals through alteration reactions (e.g., Zolotov, 2018) is suggested by the elevated bulk S
125 content measured at three landing sites (Surkov et al., 1984, 1986). The Venus atmosphere

126 contains S-bearing gas species in S-O-C-H covering a wide range of oxidation states (SO₂, COS,
127 S_n, H₂S) with the highly oxidizing SO₂ being the most abundant (e.g., Fegley, 2014; Marcq et al.,
128 2018) and therefore likely the main reactant in sulfatization reactions of Ca-bearing silicates,
129 glasses and carbonates to form anhydrite and Ca-poor silicates as suggested by thermodynamic
130 calculations (e.g., Barsukov et al., 1986, 1982, 1982; Fegley and Treiman, 1992; Klose et al.,
131 1992; Zolotov, 2018). However, the S/Ca ratio in the samples analyzed at the landing sites is
132 significantly less than unity (e.g., Zolotov and Khodakovsky, 1989; Fegley and Treiman, 1992;
133 Fegley, 2014; Zolotov, 2015), suggesting that the surface materials are not fully altered and that
134 sulfatization reactions on Venus may be relatively slow. Estimating the degree of sulfatization of
135 surface materials is hindered by the possible presence of secondary sulfides (e.g., Zolotov, 2018,
136 2019 and references therein).

137 Understanding the chemical alteration of surface rocks on Venus is crucial to better
138 constrain the composition of Venus' atmosphere and surface, the composition of the highlands,
139 and possible sources of the contrasts in radar reflectivity. Experimental studies have focused on
140 either mineral stabilities and/or basaltic compositions as reacting solids considering CO₂
141 dominated gas mixtures predominantly at 1 bar (Zolotov, 2018 and references therein), but more
142 recent studies have run experiments at pressures consistent with Venus' conditions (Aveline et
143 al., 2011; Radoman-Shaw et al., 2017; Berger et al., 2019; Teffeteller et al., 2019; Port et al.,
144 2020). A number of equilibrium chemical thermodynamic studies have considered individual gas-
145 solid reactions and fugacity diagrams involving silicates, carbonates, Fe-oxides and phosphates
146 and gas mixtures including CO₂, H₂O, CO, SO₂, COS, H₂, H₂S, HCl, and HF at temperatures
147 relevant for Venus (e.g., Adamcik and Draper, 1963; Mueller, 1964; Lewis, 1970; Lewis and
148 Kreimendahl, 1980; Fegley and Treiman, 1992; Nozette and Lewis, 1982; Zolotov et al., 1997;
149 Zolotov, 2018 and references therein; Filiberto et al., 2020). This approach may not always reflect
150 the complexity of the rocks, since reactants or products may have been consumed in reactions

151 that were not considered (e.g., Klose et al., 1992). Fewer studies calculated chemical equilibria
152 in multicomponent solid-gas systems constrained by the elemental mass balances of supposed
153 rocks and the atmosphere (e.g., Khodakovsky et al., 1979; Barsukov et al., 1982; Khodakovsky,
154 1982; Barsukov et al., 1986; Klose et al., 1992). This approach allows the prediction of equilibrium
155 mineral assemblages in a chosen gas-rock system. However, solid solutions used in
156 thermodynamic modeling have been improved since the early 90s and it is worth revisiting phase
157 equilibria modeling for Venus.

158 In this work we use whole-rock compositions of tholeiitic basalt, alkali basalt, and granite,
159 and calculate equilibrium mineral assemblages at conditions estimated at the modal planetary
160 radius and at higher elevations. We model mineral assemblages as a function of fugacities of
161 H₂O-CO₂ fluids and varying both oxygen and sulfur fugacities to identify phases that could have
162 been present if Venus contained more water at an earlier stage of its formation or preserved in
163 the subsurface. Further, we show how variations in the starting composition influence mineral
164 stabilities and predict which phases would be expected at conditions relevant for elevated terrains
165 and identify phases that could be associated with the contrast in radar reflectivity.

166

167 **2. Methods**

168 **2.1. Model Parameters**

169 Phase diagrams were calculated with the Gibbs free energy minimization software Perple_X 6.8.6
170 (Connolly, 2005) using the internally consistent thermodynamic data set of Holland and Powell
171 (2011). The oxides MnO, P₂O₅, and Cr₂O₃ were excluded from the calculations because of their
172 relatively low abundances and/or absence of good solid-solution models. All solid-solution models
173 and pure phases selected for our phase equilibria calculations are listed in Table 1. The Venus
174 atmosphere was treated as a fluid as approximation for the gas that is actually in contact with the

175 surface rocks, with its properties defined by the equation of state (Holland and Powell, 1991,
176 1998). Other gases such as N_2 are not expected to significantly influence surface alteration and
177 are therefore not considered in the model. We used two different approaches to model rock
178 alteration: (1) Calculation of phase equilibria with a H_2O-CO_2 fluid, as a function of X_{CO_2} at an
179 atmospheric pressure of 95.6 bars in the temperature range of 573-973 K to study phase stabilities
180 at conditions relevant to an ancient water-rich environment or present-day subsurface conditions
181 which may contain higher concentrations of H_2O . Oxygen fugacity is fixed by either the magnetite-
182 hematite (MH) or the quartz-fayalite-magnetite (QFM) buffers. (2) Computation of phase equilibria
183 as a function of O_2 and S_2 gas fugacities (f_{O_2} and f_{S_2}), assuming an atmosphere dominated by
184 CO_2 with 30 ppm of H_2O . In our model, fugacities of O_2 and S_2 are treated as independent
185 variables, resulting in the following additional gas components: SO_2 , CO , H_2S , H_2 , and CH_4 .
186 Fluid/gas properties of this hybrid equation of state are computed using the Compensated-
187 Redlich-Kwong (CORK) equation of state for CO_2 and H_2O (Holland and Powell, 1991, 1998) and
188 a Modified Redlich-Kwong equation of state (de Santis et al., 1974) for all components in O_2 and
189 S_2 fugacity diagrams at atmospheric pressures of 95.6 and 50 bars, respectively.

190 **2.2. Input Parameters**

191 ***2.2.1. Starting Rock Compositions***

192 Three starting rock compositions (Table 2) were used for our phase equilibria calculations: (1) a
193 synthetic tholeiitic basalt based on the Venera 14 rock analyses (Treiman, 2007) and terrestrial
194 analogs for elements not analyzed by the lander (Filiberto, 2014), which has been used as starting
195 composition in experimental studies (Teffeteller et al., 2019); (2) a natural alkali-rich basalt from
196 Sverrefjell volcano, Svalbard (Skjelkvåle et al., 1989), which is chemically similar to the Venera
197 13 analysis (Treiman, 2007); and (3) an intraplate A-type granite from Svöfjell, southern Norway

198 (Auwera et al., 2003; SV1, their table 6), which was interpreted to be derived by extreme
199 differentiation of basic magmas.

200 **2.2.2. Venus surface conditions**

201 At the elevation of the modal planetary radius (6051.37 km), temperature and pressure are 740
202 K (~467 °C) and 95.6 bars (Seiff et al., 1985). Conditions at other elevations vary in the range of
203 758-658 K and 110-47 bars. In accordance with this data, we use 740 K and 95.6 bars for
204 conditions at the basaltic plains and 660 K (~387 °C) at 50 bars as exemplary for high-elevation
205 tesserae. While today's atmosphere is dominated by CO₂, with lesser SO₂, H₂O and other gases
206 (Fegley, 2014; Marcq et al., 2018), Venus' atmosphere may have contained more H₂O early in its
207 history (Way et al., 2016; Salvador et al., 2017). Hence, OH-bearing minerals may have been
208 preserved as metastable phases or in the subsurface, where rocks are not in contact with the
209 atmosphere. Therefore, we calculate phase stabilities for the three starting compositions as a as
210 a function of X_{CO_2} ($\text{CO}_2/[\text{CO}_2+\text{H}_2\text{O}]$) within the range of 573-973 K and a saturated H₂O-CO₂ fluid
211 phase (i.e. assuming that a fluid/gas is always present in sufficient quantity to saturate the system
212 in the phase). While pressure conditions are expected to vary if the atmosphere contained more
213 H₂O, relatively small pressure changes (i.e. 50 bars) do not have a significant effect on phase
214 stability. A pressure of 95.6 bars was chosen since it also covers present-day shallow subsurface
215 conditions, where higher concentrations of water in the form of OH-bearing minerals may have
216 been preserved.

217 The oxygen fugacity of the near-surface atmosphere has been derived from the calculation
218 of chemical equilibria among atmospheric gases and lies within the range of 10^{-21.7} to 10⁻²⁰ bars
219 at modal planetary radius, which is indistinguishable from the MH phase boundary (Fegley et al.,
220 1997b, 1997a; Zolotov, 1996, 2015; Fegley, 2014). The oxidation state of basalt, however, is more
221 reduced, and ranges from near QFM on Earth to lower values on other planetary bodies (e.g.,

222 Herd, 2003; Schmidt et al., 2013). Based on these fugacities, we calculate phase equilibria using
223 QFM and MH buffers for phase diagrams in H₂O-CO₂ space. Fugacity diagrams are calculated
224 for $f_{O_2} = 10^{-30} - 10^{-15}$ bars but we focus on phases within the range of 10^{-19} to 10^{-23} bars. The
225 oxygen fugacity at higher elevations is not known due to a lack of gas equilibria (Krasnopolsky,
226 2007; Zolotov, 1996; Fegley et al., 1997a; Zolotov, 2018), which is why we assume a similar range
227 but with larger uncertainties. Calculations including sulfur fugacity (f_{S_2}) are in the range of 10^{-10}
228 to 10^{-2} bars which cover the values of $\sim 10^{-5}$ bars given by Zolotov (2018), based on 0.23 ppmv of
229 S₂ in the atmosphere corresponding to gas equilibrium concentrations at modal radius (Zolotov,
230 1996).

231

232 **3. Results**

233 **3.1. Effect of H₂O-CO₂ fluid composition on phase equilibria**

234 Figure 1 shows the calculated phase equilibria as a function of X_{CO_2} at fluid saturated conditions
235 for the three different starting rock compositions and QFM and MH f_{O_2} buffers. The molar
236 proportion of hematite component in the ilmenite-hematite solid solution is indicated by the color
237 coding and is an indicator of oxidization state.

238 Amphibole, predominantly tremolite, is the dominant hydrous phase that forms from the
239 basaltic protolith and is stable up to $X_{CO_2} \sim 0.88$ at the QFM oxidation state (Fig. 1a), and to even
240 higher values at MH (Fig. 1b). Biotite is present only in small proportions but is stable at higher
241 temperatures and higher X_{CO_2} than amphibole. Chlorite, epidote, and white mica, mostly
242 muscovite, are present in the lower temperature range of the phase diagrams. Calculations at MH
243 show talc as a stable phase; it is not calculated to be stable at QFM. The stable anhydrous mineral
244 assemblage at QFM and CO₂-rich conditions is orthopyroxene + clinopyroxene + feldspar +

245 olivine + ilmenite. At MH, a similar anhydrous assemblage is calculated, but with quartz instead
246 of olivine. Carbonate minerals (including calcite, magnesite, and dolomite) are stable below 660
247 K at QFM and even lower at MH. The proportion of hematite in the hematite-ilmenite solid-solution
248 increases with CO₂ and temperature for both f_{O_2} buffers but drops to nearly zero in the anhydrous
249 assemblage of clinopyroxene + orthopyroxene + feldspar + ilmenite ± quartz ± olivine.

250 The altered alkali basalt is calculated to contain abundant biotite at both fugacities.
251 Chlorite, epidote, and muscovite are stable at lower temperatures, while amphibole is absent. The
252 anhydrous assemblage consists of clinopyroxene + plagioclase + nepheline + leucite + ilmenite,
253 with olivine + spinel at QFM and with titanite at MH. Calcite is stable up to almost 773 K at high
254 X_{CO_2} . Analogous to the alteration of tholeiitic basalt, the proportions of hematite in the hematite-
255 ilmenite solid solution increase with higher proportions of CO₂ and temperature for both buffers.
256 However, at QFM, ilmenite is not always a stable phase and is replaced by titanite.

257 Because of its low proportions of FeO and MgO, the mineralogy of altered granite is
258 dominated by plagioclase, K-feldspar, and quartz. Biotite is the most stable hydrous phase at
259 most conditions. Epidote, chlorite, and white mica are present at lower temperatures. The
260 anhydrous mineral assemblage for QFM consists of clinopyroxene + orthopyroxene + plagioclase
261 + K-feldspar + ilmenite + quartz. At MH, the equilibrium assemblage contains titanite instead of
262 orthopyroxene. Carbonates are stable below temperatures of ~ 640 K.

263 **3.2. Effect of f_{O_2} and f_{S_2} on phase equilibria**

264 Phase diagrams for the compositions of the tholeiitic basalt, alkali basalt and granite as
265 functions of O₂ and S₂ fugacities are calculated and the results for the basalt at conditions at
266 planetary radius and higher elevations are shown in Figure 2 (phase diagrams for the alkali basalt
267 and granite compositions are available as Supplementary Fig. 1). The compositions of the gas in
268 equilibrium with the solid phases for both conditions are also shown in Fig. 2. Hematite and

269 magnetite are modeled as single phases instead of solid solutions, to show their individual stability
270 fields. Ilmenite (without hematite) is represented by an ideal solution and spinel as a solid solution
271 between MgAl_2O_4 and FeAl_2O_4 . In an additional calculation, we explore the effect of using an
272 ilmenite-hematite solid solution.

273 Figure 2a shows the calculated mineral assemblages for the tholeiite basalt protolith
274 (Table 2) as functions of $f\text{O}_2$ and $f\text{S}_2$ at the temperature and pressure of the mean planetary radius
275 (740 K, 95.6 bar). Fig. 2c shows the stabilities of the gas species in equilibrium with the solid
276 phases calculated in Fig. 2a. The dominant gas phase at most fugacities is CO_2 while only the
277 most oxidizing conditions considered are dominated by SO_2 . All other gas components are
278 present in small amounts. At oxidizing, SO_2 -dominated and at reducing conditions, H_2O is less
279 abundant than other gases. The black box represents the most likely range of oxygen (10^{-19} - 10^{-23}
280 bars) and sulfur ($10^{-4.2}$ - 10^{-6} bars) fugacities, that cover the values given by Zolotov (2018) and
281 spans the modeled MH phase boundary at an oxygen fugacity of $\sim 10^{-20.7}$ bars. In calculations
282 using a solid solution of hematite and ilmenite the MH transition is shifted to $f\text{O}_2 = 10^{-23.2}$ bars,
283 which therefore extends the stability of hematite solid solution with respect to magnetite at the
284 mean planetary radius. Pyrite is stable at $f\text{O}_2 \sim 10^{-21}$ bars and more reducing conditions at $f\text{S}_2$ in
285 the range of $10^{-5.2} - 10^{-4.1}$ bars. Pyrrhotite is not a stable phase near the mean planetary radius
286 and requires more reducing $f\text{O}_2$ ($10^{-21.5}$ bars) and $f\text{S}_2$ below $10^{-5.2}$ bars.

287 As a result of an increase of SO_2 in the gas with oxidizing conditions in the calculated
288 phase diagram, (Fig. 2c) anhydrite is stable starting at $f\text{O}_2 = 10^{-22.5}$ bars at $f\text{S}_2$ of 10^{-2} bars and $f\text{O}_2$
289 = 10^{-20} bars at $f\text{S}_2$ 10^{-10} bars and more oxidizing conditions. Since anhydrite bonds the Ca of the
290 system, clinopyroxene is not stable at these conditions and is replaced by other silicates such as
291 enstatite, quartz, and cordierite. At lower temperature and pressure conditions (Fig. 2b) the
292 transition from magnetite to hematite is shifted towards $f\text{O}_2 = 10^{-23.3}$ bars. If $f\text{O}_2$ and $f\text{S}_2$ at higher
293 elevations are comparable to those at planetary radius, hematite is expected to be the stable

294 oxide at most fugacities (black rectangle, Fig 2b). Pyrite is stable at $fO_2 \sim 10^{-22}$ bars and more
295 reducing conditions at fS_2 10^{-4} - $10^{-5.2}$ bars. Biotite is present within a small range of relatively low
296 fO_2 and fS_2 .

297 The phase relations of iron oxides and sulfides in the alkali basalt and granite are like
298 those in the tholeiite and depend only on temperature and fugacities (see Fig. 1 in supplementary
299 material). Due to differences in major oxides in the alkali basalt composition, olivine, spinel, and
300 the feldspathoid nepheline are stable in the modeled phase diagram. Biotite is stable at most
301 conditions except at SO_2 dominant and reducing conditions. Dolomite is present at high elevations
302 and at low fO_2 in our model, where SO_2 in the gas is low (and hence conditions that are not likely
303 for present-day Venus). In the granitic composition, calcite is a stable phase in our model at low
304 SO_2 . Anhydrite and silicates such as andalusite, cordierite, albite, and quartz form at SO_2 -rich
305 conditions.

306

307 **3.3. Mineral stabilities with changes in elevation**

308 In Fig. 3 we show the modeled abundances of magnetite, hematite, pyrite, and anhydrite in the
309 basaltic composition for three fO_2 and fS_2 pairs as a function of decreasing temperature (i.e.,
310 increasing elevation). While the pressure also decreases with elevation, it has a less significant
311 effect on mineral stabilities and is therefore assumed at a constant value of 90 bars. At $fO_2 = 10^{-21}$
312 and $fS_2 = 10^{-5}$, magnetite, hematite and anhydrite are present while pyrite is not stable. The
313 magnetite-hematite transition occurs at temperature conditions estimated for the mean planetary
314 radius (green box in Fig. 3). If fugacities are assumed to be constant in the atmosphere, hematite
315 and anhydrite would be the expected phases at higher elevations and pyrite would be absent.
316 However, variations in fO_2 and fS_2 (indicated by dashed lines in Fig. 3), especially somewhat
317 lower oxygen fugacities at 10^{-23} , would stabilize pyrite at higher elevations.

318

319 **4. Discussion**

320 **4.1. Limitations of our model**

321 The applicability of equilibrium thermodynamic models is mainly limited by uncertainties in
322 thermodynamic properties of minerals and their solid solutions, incomplete data of the Venus
323 atmosphere and rock compositions and the lack of equilibration between atmospheric gases
324 and/or at gas mineral interfaces.

325 Mineral stabilities in our model are influenced by uncertainties in the thermodynamic data
326 used for minerals and solid solutions. In the case of the magnetite-hematite phase boundary,
327 Fegley et al. (1997b) describe a large range of tabulated thermodynamic data for hematite and
328 magnetite, which results in the variation of calculated fO_2 by over three orders of magnitude at
329 Venus surface temperatures. The internally consistent thermodynamic data set (Holland and
330 Powell, 2011) in our model is based on data for magnetite and hematite given by Robie and
331 Hemingway (1995) and the calculated magnetite-hematite boundary in our model is therefore
332 comparable to the results of Fegley et al. (1997b). While the temperature dependence of the
333 thermal expansion and bulk modulus are modeled in a consistent way and thermodynamic models
334 are in good agreement with existing experimental results, uncertainties remain due to missing
335 calorimetric and experimental data and the use of fictive end-members used in some solid
336 solutions (e.g., Holland and Powell, 2011).

337 The clinopyroxene solid solution model used in our computations does not incorporate
338 titanium, which may result in an increased stability field and higher abundances of titanium-
339 bearing phases such as ilmenite and rutile. Furthermore, we do not consider Mn, P, and Cr, which
340 may shift mineral reactions and stability fields. Halogen gases such as HCl and HF, which have

341 been detected spectroscopically in the Venus atmosphere, are also not considered in our model
342 but they not expected to influence mineral stabilities due to their low partial pressures (Zolotov,
343 2018). However, HCl can affect Na/K carbonates (Zolotov, 2018), which may not be present at
344 surface conditions and also have not been considered in our model, but they are not expected to
345 influence mineral stabilities die to their low partial pressures (Zolotov, 2018). However, HCL can
346 affect Na/K carbonates (Zolotov, 2018), which may not be present at surface conditions and also
347 have not been considered in our model. Furthermore, the gas composition does not include all
348 species measured in the Venus atmosphere and the influence of these gas species (COS, S_n)
349 are currently not modeled.

350 The thermodynamic data base currently does not include Na- or K-bearing sulfates and
351 their stabilities could therefore not be explored in our model. Experiments have reported Na-Ca
352 sulfates as alteration products (e.g., Berger et al., 2019) and we would therefore expect their
353 presence in the SO₂ dominant section of the phase diagram, together with anhydrite.

354 Major element geochemistry from the Venera and Vega landers show large error bars
355 compared with terrestrial analyses and are also incomplete (Surkov et al., 1984, 1986; Kargel et
356 al., 1993; Grimm and Hess, 1997; Treiman, 2007). Variations in the whole-rock starting
357 composition are expected to influence stabilities and proportions of minerals in our equilibrium
358 approach. Large uncertainties are also recorded for atmospheric gas species in particular
359 tropospheric H₂O, which shows significant variations and errors at altitudes from 0-15 km (Marcq
360 et al., 2018 and references therein).

361 The results obtained by phase equilibria calculations assume equilibrium at all conditions
362 considered. This implies that mineral assemblages described in this study are only present after
363 reaching complete equilibrium with the modeled gas composition. While temperatures on Venus
364 are sufficiently high for reactions and Venus rocks have been exposed to the atmosphere over

365 geological time scales, liquid, or supercritical water (dense solvents) are absent. In CO₂
366 dominated fluids, the breakdown of silicate structures may be impeded due to the very low
367 dielectric constant despite favorable Gibbs free energy of reactions. However, experimental work
368 has shown that silicate alteration occurs when SO₂ is present, but at different conditions than
369 estimated for present-day Venus (Delmelle et al., 2018; King et al., 2018; Palm et al., 2018;
370 Renggli and King, 2018). Oxidation of glasses is limited by the rate of chemical diffusion of cations
371 such as Fe²⁺, Ca²⁺, Mg²⁺ and Na⁺ towards the free mineral surface rather than the diffusion of
372 gases (e.g., Berger et al., 2019; Zolotov, 2018 and references therein). However, kinetic
373 constraints on solid-gas reactions are poorly constrained and require more experimental
374 evaluations at Venus conditions (Zolotov, 2018).

375 Furthermore, reaction rates vary and phases such as olivine may be more reactive than
376 others (e.g., clinopyroxene or feldspars) as suggested by the amount of S detected by surface
377 probes indicating ongoing and incomplete alteration of primary Ca-bearing minerals (except for
378 plagioclase of intermediate composition) in basalt (e.g., Barsukov et al., 1986; Zolotov, 2015) and
379 experimental studies (e.g., Radoman-Shaw et al., 2017; Berger et al., 2019; Filiberto et al., 2020).
380 The surface rocks on Venus consists of a mixture of incompletely reacted minerals from the
381 primary igneous rocks with newly formed alteration products as a result of gas-solid reactions
382 (Klose et al., 1992). While phase equilibria models cannot reflect the kinetic restrictions, they still
383 can be a helpful tool to understand, which mineral phases are likely to be expected.

384 While thermochemical equilibrium is generally assumed for near-surface conditions at
385 planetary radius (Krasnopolsky and Parshev, 1981; Krasnopolsky, 2007; Fegley et al., 1997a),
386 elevated terrains are likely exposed to gases in disequilibrium and gas compositions that differ
387 from those at modal radius (Zolotov, 1996, 2018). Due to the lack of chemical gas equilibrium,
388 f_{O_2} and fugacities of certain undetected/uncertain gases (e.g., H₂, S₂, H₂S) at higher elevations

389 cannot be evaluated by thermodynamic methods making the prediction of minerals by equilibrium
390 calculations less reliable than for conditions at planetary radius.

391 Modeling equilibrium reactions is more applicable to homogeneous materials such as
392 volcanic/impact glasses instead of rocks with large mineral grains that will alter individually at
393 limited solid-solid diffusion (e.g., Zolotov and Volkov, 1992). Furthermore, the higher reactivity of
394 some minerals with respect to others may lead to different alteration product than shown in our
395 equilibrium approach.

396

397 **4.2. Comparison to other thermodynamic models**

398 Only a few studies used the calculations of chemical equilibria in multicomponent gas-solid type
399 systems to study alteration processes on Venus. Khodakovsky et al. (1979) calculated the
400 equilibrium mineralogy for a range of rock compositions, but did not include sulfur compounds
401 and did not consider solid solutions. Below, we compare their results to our sulfur-free H₂O-CO₂
402 fluid calculations. In addition, Barsukov et al. (1982, 1986), Khodakovsky et al. (1982), and Klose
403 and Zolotov (1992), used Gibbs free energy minimization models with S-bearing gases. While
404 general comparisons are possible, each of these studies used a different approach representing
405 atmospheric conditions, which results in variations in mineral abundances.

406 Khodakovsky et al. (1979) reported that their equilibrium modeling of a basalt composition
407 (for elevations up to 5 km) yielded glaucophane, epidote, and annite as main hydrous phases with
408 traces of chloritoid. For their sodium alkaline and potassium alkaline lavas, they predict relatively
409 large amounts of glaucophane and phlogopite with lesser amounts of tremolite at lower
410 temperature conditions as well as calcite, dolomite and epidote predominantly in the sodium
411 alkaline lavas (Khodakovsky et al., 1979). In the rhyolite composition, they predict small amounts
412 of glaucophane, chloritoid, and epidote. In our H₂O-CO₂ fluid model, amphibole is the abundant

413 hydrous phase in basalt, but the amphibole composition is dominated by tremolite component
414 instead of glaucophane; glaucophane is stable only at very high pressures, > 11 kilobars at
415 temperatures > 800 K (Corona and Jenkins, 2007; Evans, 2007). Furthermore, our results do not
416 suggest epidote to be stable in the basalt at increasing CO₂. Instead, we predict talc and chlorite
417 as hydrous phases depending on X_{CO₂} and oxygen buffers in the basalt. In the granite, however,
418 epidote is stable X_{CO₂} < 0.8. Biotite is mostly present in the alkali basalt and the granite. We do
419 not report chloritoid in any composition, which is generally not a relevant phase in altered igneous
420 rocks.

421 Previous energy minimization studies that include sulfur-containing species (Barsukov et
422 al., 1982; Klose et al., 1992; Treiman and Schwenzer, 2009), report plagioclase, orthopyroxene,
423 clinopyroxene, K-feldspar, quartz, and anhydrite at various conditions. Our results agree with
424 those of Klose et al. (1992), with orthopyroxene and anhydrite forming at the expense of anorthite
425 and clinopyroxene (diopside) at higher oxygen fugacities. However, they find andalusite to be the
426 product of this reaction, whereas our model prefers cordierite in the basalt and alkali basalt
427 compositions, and cordierite with andalusite in the granite. Barsukov et al. (1982) report small
428 amounts of cordierite as a calculated product from their granitic protolith. Our results agree with
429 those of Treiman and Schwenzer (2009), finding cordierite rather than andalusite to be the
430 dominant phase when calculating phase equilibria using bulk rock compositions and solid
431 solutions. This is also supported in results presented by Klose and Zolotov (1992), where
432 andalusite is not a stable phase when solid solution models are considered.

433 All energy minimization models report the presence of iron-bearing phases such as
434 magnetite, hematite, and pyrite. Barsukov et al. (1982) calculated the presence of either
435 magnetite or pyrite in basalts and granites at the mean planetary radius. Klose et al. (1992),
436 calculated that magnetite is stable rather than pyrite at mean radius conditions, but concluded
437 that the magnetite/pyrite phase boundary varies with the redox state of the atmosphere, and

438 stabilizes pyrite only at higher elevations. Our model agrees with their findings supporting the
439 stability of either magnetite, hematite, or both at planetary radius, while pyrite should be present
440 at higher elevation where sulfur- and oxygen-fugacities may vary. Zolotov (1994) concluded that
441 hematite solid solutions with ilmenite and geikielite are stable to lower fO_2 than pure hematite,
442 which is in agreement with our results in calculations using ilmenite-hematite solid solutions.
443 Pyrrhotite is only stable at reduced conditions according to Klose et al. (1992), and is not likely a
444 relevant phase at present Venus conditions, which is in agreement with our results.

445 Klose et al. (1992) found rutile to be the Ti-bearing mineral in the basalt, which is in
446 accordance with our results. Barsukov et al. (1982) reported either titanite or no Ti phase. We find
447 titanite stable in the alkali basalt and granite compositions at low oxygen fugacities, but it is
448 replaced by rutile with increasing oxidation state. Klose et al. (1992) found spinel and corundum
449 in their basaltic composition, while Barsukov et al. (1982) reported hercynite. Neither spinel nor
450 corundum are stable in our basaltic compositions, although spinel as solid solution is found in the
451 alkali basalt. Olivine and nepheline are also stable in the phase diagram of the alkali basalt
452 composition.

453 Neither study that considered sulfur-bearing species found that calcite would be stable at
454 conditions of either the mean radius or higher elevations. Our results agree with these findings.
455 However, we report the stability of dolomite in the alkali basalt, and calcite in the granite at low
456 oxygen- and relatively high sulfur fugacities as a result of low fSO_2/fS_2 and therefore outside the
457 range of anhydrite stability.

458

459 **4.3. Comparison to experimental data**

460 A large number of experimental works have studied gas-solid reactions at Venus conditions using
461 either minerals or rocks as reacting solids, a variety of gas mixtures, and varying pressure-

462 temperature conditions (see Zolotov, 2018 for a review). It is beyond the scope of this paper to
463 discuss the differences in experimental conditions and results, we will focus on general
464 observations. Most studies report the formation of Fe-oxides such as magnetite and/or hematite
465 during the alteration of basaltic compositions and particularly olivine in a CO₂-rich environment
466 (e.g., Fegley et al., 1995a; Berger et al., 2019; Teffeteller et al., 2019). Our results agree with
467 these findings: both magnetite and hematite are thermodynamically stable on Venus and their
468 presence would depend on oxygen fugacity, which is currently poorly constrained.

469 In the presence of sulfur-bearing gases, the majority of experimental studies suggest the
470 reaction of Ca-bearing carbonates and other Ca-bearing phases such as pyroxenes to form
471 anhydrite and other Na/Ca-bearing sulfates (Fegley and Prinn, 1989; Aveline et al., 2011;
472 Radoman-Shaw et al., 2017; Berger et al., 2019). While anhydrite seems to be the most common
473 mineral in experimental studies, thenardite and glauberite also form from Na-bearing basaltic
474 glass under oxidizing conditions relevant for Venus (Berger et al., 2019) and Earth (Palm et al.,
475 2018; Renggli and King, 2018). The thermochemical databases that we used do not include Na-
476 bearing sulfates, but we predict the presence of anhydrite at most Venus conditions, which agrees
477 with experimental results. Sulfatization reactions occur within hours to days on laboratory
478 timescales and therefore would be expected to go rapidly to completion on the surface of Venus.
479 However, the chemical compositions of Venus surface materials do not show that all their Ca was
480 converted to CaSO₄ (e.g., Barsukov et al., 1986; Fegley and Treiman, 1992; Zolotov and Volkov,
481 1992), which suggests that anhydrite formation is relatively slow on Venus' surface (Gilmore et
482 al., 2017). Experimental data implies the migration of Ca and Na to form sulfates on the surface
483 of the solid material and possibly suppressed recrystallization of silicates below surfaces (Zolotov,
484 2018). Diffusional transport mechanics therefore seem to be rate controlling factors for the
485 formation of sulfates (Renggli and King, 2018) and reactions may slow down once the surface
486 layer has reacted with the atmosphere and the transport of elements is less feasible. Alternatively,

487 the observed S/Ca atomic ratios <1 could be the result of Ca-Na plagioclase being stable with
488 respect to sulfatization (e.g., Zolotov, 2018). Our model assumes equilibrium conditions with the
489 formation of anhydrite going to completion together with cordierite and quartz as additional
490 reaction products, which are not likely to be expected on the surface if reactions are limited by
491 diffusion.

492 The stability of sulfides remains a controversial issue in experimental studies, which is
493 mainly due to significant uncertainties in abundances of S_2 , COS, H_2S , and CO in the lower
494 atmosphere (Marcq et al., 2018; Johnson and Oliveira, 2019) as well as in the reaction chambers
495 and variety in gases used to assess the stability of sulfide minerals. Several experimental studies
496 found that pyrite was not stable on Venus' surface and suggested pyrrhotite might be stable
497 instead (Fegley and Treiman, 1992; Fegley, 1997; Fegley et al., 1997b; Hong and Fegley, 1998,
498 1997; Fegley et al., 1995b). In contrast, Port et al. (2016) found that pyrite could be stable. Berger
499 et al. (2019) found pyrite in an experimental run that was exposed to accidental cooling, which
500 could indicate pyrite stability at higher elevations although the concentrations of S-bearing gases
501 were uncertain in their experiments. Sulfide stability is strongly dependent on the composition of
502 the atmosphere (Zolotov, 2019), and our results confirm that even small changes in the fugacities
503 of sulfur and oxygen gas can have strong effects on the stability of pyrite. Without more precise
504 and accurate constraints on composition of Venus' atmosphere near its surface, we cannot make
505 any definite predictions about the stability of sulfides on Venus.

506 **4.4. Water-bearing phases on Venus**

507 The abundance of H_2O is very low in today's atmosphere, ~ 30 ppm (Fegley, 2014; Marcq et al.,
508 2018; Zolotov, 2018) but it has been argued that Venus has lost a significant amount of water
509 throughout its history based on the high deuterium-hydrogen ratio measured in the Venusian
510 atmosphere (Donahue et al., 1982; Kumar and Taylor, 1985b; Bergh et al., 1991; Krasnopolsky,

511 2010). How Venus transitioned from a possibly water-bearing to a water-poor and hot atmosphere
512 is not known and models have suggested a rapid loss (Kasting and Pollack, 1983; Kasting, 1988),
513 a monotonic decline (Grinspoon, 1993), or a sporadic decline (Grinspoon and Bullock, 2007). In
514 particular a sporadic decline model (Grinspoon and Bullock, 2007) could have caused more
515 recent fluctuations in atmospheric H₂O and hence resulted in the formation of OH-bearing phases.
516 Our model shows that OH-bearing phases can form in a predominantly CO₂-rich environment with
517 only a small proportion of H₂O present. Experiments with added H₂O do show the formation of
518 amphibole (hornblende), chlorite, and celadonite (Berger et al., 2019), phases that are also
519 common in our thermodynamic models. While the present surface conditions would likely have
520 resulted in the dehydration of these phases, they may have been present during an earlier stage
521 of Venus or still exist in the subsurface that is not in contact with the atmosphere (Zolotov, 2018).
522 However, decomposition experiments have shown that tremolite could survive over geological
523 time scales under Venus surface conditions (Johnson and Fegley, 2000, 2003a, 2003b).

524

525 **4.5. Radar anomalies at higher elevations**

526 The nature of the high radar backscatter material at higher elevations is still a matter of debate.
527 Here, we only discuss the relevance of our model for the radar anomalies in the northern latitude
528 since we have not considered ferroelectric materials that can explain the radar behavior at Ovda
529 Regio and other equatorial highlands (Treiman et al., 2016). A number of materials have been
530 suggested as cause for the high radar backscatter at Maxwell Montes, including semiconductor
531 minerals such as pyrite (Ford and Pettengill, 1983; Klose et al., 1992; Pettengill et al., 1992, 1996;
532 Wood, 1997), although a relatively large amount would be required to match the permittivity
533 values (Gilmore et al., 2017). The stability of pyrite on Venus' highlands, however, was questioned
534 since the atmosphere was considered too oxidizing (Fegley et al., 1997b) and other substances

535 were suggested including perovskite (Fegley et al., 1992), chalcogenide compounds (Brackett et
536 al., 1995), and ‘heavy metal frosts’ (Pettengill et al., 1996; Schaefer and Fegley, 2004). The
537 elements in most of these compounds are rare in the solar system, and particularly so in igneous
538 rocks (e.g., Bi, Te, Nb), and would therefore require significant enrichment processes to be
539 present in abundances that match the radar properties (Treiman et al., 2016; Gilmore et al., 2017).
540 Furthermore, experimental studies have shown that many of these are not stable at highland
541 surface conditions, or are stable at all Venus conditions and can therefore not explain the changes
542 in radar reflectivity with elevation (Kohler et al., 2012, 2013, 2014; Guandique et al., 2014; Port et
543 al., 2020).

544 Results of our work are consistent with earlier suggestions that pyrite could be stable at
545 higher elevation. Furthermore, at specific oxygen- and sulfur fugacities, pyrite transitions to
546 hematite at higher elevations (Fig. 3), which could provide an alternative explanation for the
547 sudden drop in radar brightness in certain regions. Therefore, we suggest that pyrite could cause
548 the high radar backscatter material on Maxwell Montes and possibly other high elevation areas.

549 **5. Conclusions**

550 We used calculations of equilibrium mineral assemblages in multi-component gas-solid systems
551 open with respect to CO₂, O₂, and S₂ gases to model rock-atmosphere reactions at Venus surface
552 conditions for whole rock compositions ranging from basaltic to granitic. In sulfur-free model runs
553 with CO₂-H₂O fluids that could possibly reflect an early, water-rich Venus ore present-day
554 subsurface, amphibole and biotite are the dominant Oh-bearing minerals but are replaced by H-
555 free assemblages at high X_{CO₂}. Calcite may occur at lower temperature in the alkali-rich basalt.
556 At high fSO₂, however, Ca-carbonates are not stable at conditions of planetary radius and instead
557 replaced by anhydrite. The stabilities of Fe-oxides and sulfides are very sensitive to variations in
558 atmospheric composition and fugacities that are currently not well known for the surface of Venus.

559 However, even when considering a larger range of oxygen and sulfur fugacities, our work is
560 consistent with previous findings that conditions at the modal planetary radius are close to the
561 magnetite-hematite transition for all considered rock types, while the assemblage of hematite +
562 anhydrite ± pyrite may be more likely at lower temperatures (and pressures). The presence of
563 pyrite may therefore be responsible for the observed radar brightness of some mountain tops,
564 negating the need for highly uncommon phases such as chalcogenides and 'heavy metal frosts'.

565

566 **Acknowledgements:** This work was partially funded by NASA grant SSW#80NSSC17K0766. M.
567 Zolotov and G. Berger are thanked for their detailed reviews that greatly improved an earlier
568 version of this manuscript. O. Aharonson is thanked for editorial handling. This is LPI contribution
569 number 2348.

570

571 **References**

- 572 Adamcik, J.A., Draper, A.L., 1963. The temperature dependence of the Urey equilibrium and the problem
573 of the carbon dioxide content of the atmosphere of Venus. *Planetary and Space Science* 11,
574 1303–1307. [https://doi.org/10.1016/0032-0633\(63\)90235-6](https://doi.org/10.1016/0032-0633(63)90235-6)
- 575 Arvidson, R.E., Brackett, R.A., Shepard, M.K., Izenberg, N.R., Fegley, B., Plaut, J.J., 1994. Microwave
576 Signatures and Surface Properties of Ovda Regio and Surroundings, Venus. *Icarus* 112, 171–186.
577 <https://doi.org/10.1006/icar.1994.1176>
- 578 Auwera, J.V., Bogaerts, M., Liégeois, J.-P., Demaiffe, D., Wilmart, E., Bolle, O., Duchesne, J.C., 2003.
579 Derivation of the 1.0–0.9 Ga ferro-potassic A-type granitoids of southern Norway by extreme
580 differentiation from basic magmas. *Precambrian Research, Origin and Evolution of Precambrian*
581 *Anorogenic Magmatism* 124, 107–148. [https://doi.org/10.1016/S0301-9268\(03\)00084-6](https://doi.org/10.1016/S0301-9268(03)00084-6)
- 582 Aveline, D.C., Abbey, W.J., Choukroun, M., Treiman, A.H., Dyar, M.D., Smrekar, S.E., Feldman, S.M.,
583 2011. Rock and mineral weathering experiments under model Venus conditions. Presented at
584 the 42nd Lunar and Planetary Science Conference. Abstract #2165.
- 585 Barsukov, V.L., Borunov, S.P., Volkov, V.P., Dorofeeva, V.A., Zolotov, M.I., 1986. Analysis of the mineral
586 composition of soil at the landing sites of the Venera-13, Venera-14, and Vega-2 landers on the
587 basis of thermodynamic calculations. *Akademiia Nauk SSSR Doklady (in Russian)* 287, 415.
- 588 Barsukov, V.L., Volkov, V.P., Khodakovsky, I.L., 1982. The crust of Venus: Theoretical models of chemical
589 and mineral composition. *Journal of Geophysical Research: Solid Earth* 87, A3–A9.
590 <https://doi.org/10.1029/JB087iS01p000A3>

591 Basilevsky, A.T., Nikolaeva, O.V., Weitz, C.M., 1992. Geology of the Venera 8 landing site region from
592 Magellan data: Morphological and geochemical considerations. *Journal of Geophysical*
593 *Research: Planets* 16315–16335. [https://doi.org/10.1029/92JE01557@10.1002/\(ISSN\)2169-](https://doi.org/10.1029/92JE01557@10.1002/(ISSN)2169-9100.MAGELLAN1)
594 9100.MAGELLAN1

595 Basilevsky, A.T., Shalygin, E.V., Titov, D.V., Markiewicz, W.J., Scholten, F., Roatsch, Th., Kreslavsky, M.A.,
596 Moroz, L.V., Ignatiev, N.I., Fiethé, B., Osterloh, B., Michalik, H., 2012. Geologic interpretation of
597 the near-infrared images of the surface taken by the Venus Monitoring Camera, Venus Express.
598 *Icarus, Advances in Venus Science* 217, 434–450. <https://doi.org/10.1016/j.icarus.2011.11.003>

599 Berger, G., Cathala, A., Fabre, S., Borisova, A.Y., Pages, A., Aigouy, T., Esvan, J., Pinet, P., 2019.
600 Experimental exploration of volcanic rocks-atmosphere interaction under Venus surface
601 conditions. *Icarus* 329, 8–23. <https://doi.org/10.1016/j.icarus.2019.03.033>

602 Bergh, C.D., Bézard, B., Owen, T., Crisp, D., Maillard, J.-P., Lutz, B.L., 1991. Deuterium on Venus:
603 Observations from Earth. *Science* 251, 547–549. <https://doi.org/10.1126/science.251.4993.547>

604 Brackett, R.A., Fegley, B., Arvidson, R.E., 1995. Volatile transport on Venus and implications for surface
605 geochemistry and geology. *Journal of Geophysical Research: Planets* 100, 1553–1563.
606 <https://doi.org/10.1029/94JE02708>

607 Campbell, B.A., Arvidson, R.E., Shepard, M.K., Brackett, R.A., 1997. Remote sensing and surface
608 properties, in: Bougher, S.W., Hunten, D.M., Phillips, R.J. (Eds.), *Venus II, Space Science Series*.
609 University of Arizona Press, Tucson, pp. 503–526.

610 Connolly, J.A.D., 2005. Computation of phase equilibria by linear programming: A tool for geodynamic
611 modeling and its application to subduction zone decarbonation. *EPSL* 236, 524–541.
612 <https://doi.org/10.1016/j.epsl.2005.04.033>

613 Corona, J.C., Jenkins, D.M., 2007. An experimental investigation of the reaction: glaucophane + 2 quartz
614 = 2 albite + talc. *European Journal of Mineralogy* 147–158. [https://doi.org/10.1127/0935-](https://doi.org/10.1127/0935-1221/2007/0019-1719)
615 1221/2007/0019-1719

616 de Santis, R., Breedveld, G.J.F., Prausnitz, J.M., 1974. Thermodynamic properties of aqueous gas
617 mixtures at advanced pressures. *Ind. Eng. Chem. Proc. Des. Dev.* 13, 374–377.
618 <https://doi.org/10.1021/i260052a013>

619 Delmelle, P., Wadsworth, F.B., Maters, E.C., Ayris, P.M., 2018. High temperature reactions between
620 gases and ash particles in volcanic eruption plumes. *Reviews in Mineralogy and Geochemistry*
621 84, 285–308. <https://doi.org/10.2138/rmg.2018.84.8>

622 Donahue, T.M., Hoffman, J.H., Hodges, R.R., Watson, A.J., 1982. Venus was wet: A measurement of the
623 ratio of deuterium to hydrogen. *Science* 216, 630–633.
624 <https://doi.org/10.1126/science.216.4546.630>

625 Esposito, L.W., Bertaux, J.-L., Krasnopolsky, V.A., Moroz, V.I., Zasova, L.V., 1997. Chemistry of the lower
626 atmosphere and clouds, in: Bougher, S.W., Hunten, D.M., Phillips, R.J. (Eds.), *Venus II: Geology,*
627 *Geophysics, Atmosphere, and Solar Wind Environment*. University of Arizona Press, Tucson, p.
628 415.

629 Evans, B.W., 2007. The synthesis and stability of some end-member amphiboles. *Reviews in Mineralogy*
630 *and Geochemistry* 67, 261–286. <https://doi.org/10.2138/rmg.2007.67.7>

631 Fegley, B., 2014. Venus, in: Holland, H.D., Turekian, K.K. (Eds.), *Treatise on Geochemistry (Second*
632 *Edition)*. Pergamon, Oxford, pp. 127–148. <https://doi.org/10.1016/B978-0-08-095975-7.00122-4>

633 Fegley, B., 1997. Why pyrite is unstable on the surface of Venus. *Icarus* 128, 474–479.
634 <https://doi.org/10.1006/icar.1997.5744>

635 Fegley, B., Klingelhöfer, G., Brackett, R.A., Izenberg, N., Kremser, D.T., Lodders, K., 1995a. Basalt
636 oxidation and the formation of hematite on the surface of Venus. *Icarus* 118, 373–383.
637 <https://doi.org/10.1006/icar.1995.1197>

638 Fegley, B., Klingelhöfer, G., Lodders, K., Widemann, T., 1997a. Geochemistry of surface-atmosphere
639 interactions on Venus, in: *Venus II: Geology, Geophysics, Atmosphere, and Solar Wind*
640 *Environment*. pp. 591–636.

641 Fegley, B., Lodders, K., Treiman, A.H., Klingelhöfer, G., 1995b. The rate of pyrite decomposition on the
642 surface of Venus. *Icarus* 115, 159–180. <https://doi.org/10.1006/icar.1995.1086>

643 Fegley, B., Prinn, R.G., 1989. Estimation of the rate of volcanism on Venus from reaction rate
644 measurements. *Nature* 337, 55–58. <https://doi.org/10.1038/337055a0>

645 Fegley, B., Treiman, A.H., 1992. Chemistry of atmosphere-surface interactions on Venus and Mars.
646 Washington DC American Geophysical Union Geophysical Monograph Series 66, 7–71.
647 <https://doi.org/10.1029/GM066p0007>

648 Fegley, B., Treiman, A.H., Sharpton, V.L., 1992. Venus surface mineralogy: Observational and theoretical
649 constraints, in: *Lunar and Planetary Science Conference Proceedings, Volume 22*. pp. 3–19.

650 Fegley, B., Zolotov, M.Yu., Lodders, K., 1997b. The oxidation state of the lower atmosphere and surface
651 of Venus. *Icarus* 125, 416–439. <https://doi.org/10.1006/icar.1996.5628>

652 Filiberto, J., 2014. Magmatic diversity on Venus: Constraints from terrestrial analog crystallization
653 experiments. *Icarus* 231, 131–136. <https://doi.org/10.1016/j.icarus.2013.12.003>

654 Filiberto, J., Trang, D., Treiman, A.H., Gilmore, M.S., 2020. Present-day volcanism on Venus as evidenced
655 from weathering rates of olivine. *Science Advances* 6, eaax7445.
656 <https://doi.org/10.1126/sciadv.aax7445>

657 Ford, P.G., Pettengill, G.H., 1983. Venus: Global surface radio emissivity. *Science* 220, 1379–1381.
658 <https://doi.org/10.1126/science.220.4604.1379>

659 Garvin, J.B., Head, J.W., Pettengill, G.H., Zisk, S.H., 1985. Venus global radar reflectivity and correlations
660 with elevation. *Journal of Geophysical Research: Solid Earth* 90, 6859–6871.
661 <https://doi.org/10.1029/JB090iB08p06859>

662 Gilmore, M.S., Mueller, N., Helbert, J., 2015. VIRTIS emissivity of Alpha Regio, Venus, with implications
663 for tessera composition. *Icarus* 254, 350–361. <https://doi.org/10.1016/j.icarus.2015.04.008>

664 Gilmore, M.S., Treiman, A.H., Helbert, J., Smrekar, S., 2017. Venus surface composition constrained by
665 observation and experiment. *Space Sci Rev* 212, 1511–1540. [https://doi.org/10.1007/s11214-](https://doi.org/10.1007/s11214-017-0370-8)
666 [017-0370-8](https://doi.org/10.1007/s11214-017-0370-8)

667 Grimm, R.E., Hess, P.C., 1997. The Crust of Venus, in: Bougher, S.W., Hunten, D.M., Phillips, R.J. (Eds.),
668 *Venus II: Geology, Geophysics, Atmosphere, and Solar Wind Environment, Space Science Series*.
669 University of Arizona Press, Tucson, pp. 1205–1244.

670 Grinspoon, D.H., 1993. Implications of the high D/H ratio for the sources of water in Venus' atmosphere.
671 *Nature* 363, 428–431. <https://doi.org/10.1038/363428a0>

672 Grinspoon, D.H., Bullock, M.A., 2007. Astrobiology and Venus Exploration, in: Esposito, L.W., Stofan,
673 E.R., Cravens, T.E. (Eds.), *Exploring Venus as a Terrestrial Planet, Geophysical Monograph Series*
674 176. American Geophysical Union, Washington, D. C., pp. 191–206.
675 <https://doi.org/10.1029/176GM12>

676 Guandique, J., Kohler, E., Chevrier, V., 2014. Stability of metallic minerals under venusian surface
677 temperatures: Investigating the potential source of radar anomalies. Presented at the 45th
678 Lunar and Planetary Science Conference. Abstract #2391.

679 Hashimoto, G.L., Roos-Serote, M., Sugita, S., Gilmore, M.S., Kamp, L.W., Carlson, R.W., Baines, K.H.,
680 2008. Felsic highland crust on Venus suggested by Galileo Near-Infrared Mapping Spectrometer
681 data. *Journal of Geophysical Research: Planets* 113, E00B24.
682 <https://doi.org/10.1029/2008JE003134>

683 Head, J.W., Crumpler, L.S., Aubele, J.C., Guest, J.E., Saunders, R.S., 1992. Venus volcanism: Classification
684 of volcanic features and structures, associations, and global distribution from Magellan data.
685 *Journal of Geophysical Research: Planets* 97, 13153–13197. <https://doi.org/10.1029/92JE01273>

686 Helbert, J., Müller, N., Kostama, P., Marinangeli, L., Piccioni, G., Drossart, P., 2008. Surface brightness
687 variations seen by VIRTIS on Venus Express and implications for the evolution of the Lada Terra
688 region, Venus. *Geophysical Research Letters* 35. <https://doi.org/10.1029/2008GL033609>
689 Herd, C.D.K., 2003. The oxygen fugacity of olivine-phyric martian basalts and the components within the
690 mantle and crust of Mars. *Meteoritics & Planetary Science* 38, 1793–1805.
691 <https://doi.org/10.1111/j.1945-5100.2003.tb00015.x>
692 Holland, T., Powell, R., 1991. A Compensated-Redlich-Kwong (CORK) equation for volumes and fugacities
693 of CO₂ and H₂O in the range 1 bar to 50 kbar and 100–1600°C. *Contributions to Mineralogy and*
694 *Petrology* 109, 265–273. <https://doi.org/10.1007/BF00306484>
695 Holland, T.J.B., Powell, R., 2011. An improved and extended internally consistent thermodynamic
696 dataset for phases of petrological interest, involving a new equation of state for solids. *J.*
697 *Metamorph. Geol.* 29, 333–383. <https://doi.org/j.1525-1314.2010.00923.x>
698 Holland, T.J.B., Powell, R., 1998. An internally consistent thermodynamic data set for phases of
699 petrological interest. *Journal of Metamorphic Geology* 16, 309–343.
700 Hong, Y., Fegley, B., 1998. The sulfur vapor pressure over pyrite on the surface of Venus. *Planetary and*
701 *Space Science* 46, 683–690. [https://doi.org/10.1016/S0032-0633\(97\)00127-X](https://doi.org/10.1016/S0032-0633(97)00127-X)
702 Hong, Y., Fegley, B., 1997. The kinetics and mechanism of pyrite thermal decomposition. *Berichte der*
703 *Bunsengesellschaft für physikalische Chemie* 101, 1870–1881.
704 <https://doi.org/10.1002/bbpc.19971011212>
705 Ivanov, M.A., Head, J.W., 2011. Global geological map of Venus. *Planetary and Space Science, Exploring*
706 *Phobos* 59, 1559–1600. <https://doi.org/10.1016/j.pss.2011.07.008>
707 Ivanov, M.A., Head, J.W., 1996. Tessera terrain on Venus: A survey of the global distribution,
708 characteristics, and relation to surrounding units from Magellan data. *Journal of Geophysical*
709 *Research: Planets* 101, 14861–14908. <https://doi.org/10.1029/96JE01245>
710 Johnson, N.M., Fegley, B., 2003a. Tremolite decomposition on Venus II. Products, kinetics, and
711 mechanism. *Icarus* 164, 317–333. [https://doi.org/10.1016/S0019-1035\(03\)00102-7](https://doi.org/10.1016/S0019-1035(03)00102-7)
712 Johnson, N.M., Fegley, B., 2003b. Longevity of fluorine-bearing tremolite on Venus. *Icarus* 165, 340–348.
713 [https://doi.org/10.1016/S0019-1035\(03\)00212-4](https://doi.org/10.1016/S0019-1035(03)00212-4)
714 Johnson, N.M., Fegley, B., 2000. Water on Venus: New insights from tremolite decomposition. *Icarus*
715 146, 301–306. <https://doi.org/10.1006/icar.2000.6392>
716 Johnson, N.M., Oliveira, M.R.R. de, 2019. Venus atmospheric composition in situ data: A compilation.
717 *Earth and Space Science* 6, 1299–1318. <https://doi.org/10.1029/2018EA000536>
718 Kargel, J.S., Komatsu, G., Baker, V.R., Strom, R.G., 1993. The volcanology of Venera and VEGA landing
719 sites and the geochemistry of Venus. *Icarus* 103, 253–275.
720 <https://doi.org/10.1006/icar.1993.1069>
721 Kasting, J.F., 1988. Runaway and moist greenhouse atmospheres and the evolution of Earth and Venus.
722 *Icarus* 74, 472–494. [https://doi.org/10.1016/0019-1035\(88\)90116-9](https://doi.org/10.1016/0019-1035(88)90116-9)
723 Kasting, J.F., Pollack, J.B., 1983. Loss of water from Venus. I. Hydrodynamic escape of hydrogen. *Icarus*
724 53, 479–508. [https://doi.org/10.1016/0019-1035\(83\)90212-9](https://doi.org/10.1016/0019-1035(83)90212-9)
725 Khodakovsky, I.L., 1982. Atmosphere-surface interactions on Venus and implications for atmospheric
726 evolution. *Planetary and Space Science* 30, 803–817. [https://doi.org/10.1016/0032-](https://doi.org/10.1016/0032-0633(82)90113-1)
727 [0633\(82\)90113-1](https://doi.org/10.1016/0032-0633(82)90113-1)
728 Khodakovsky, I.L., Volkov, V.P., Sidorov, Yu.I., Borisov, M.V., 1979. Venus: Preliminary prediction of the
729 mineral composition of surface rocks. *Icarus* 39, 352–363. [https://doi.org/10.1016/0019-](https://doi.org/10.1016/0019-1035(79)90146-5)
730 [1035\(79\)90146-5](https://doi.org/10.1016/0019-1035(79)90146-5)
731 King, P.L., Wheeler, V.M., Renggli, C.J., Palm, A.B., Wilson, S.A., Harrison, A.L., Morgan, B., Nekvasil, H.,
732 Troitzsch, U., Mernagh, T., Yue, L., Bayon, A., DiFrancesco, N.J., Baile, R., Kreider, P., Lipiński, W.,
733 2018. Gas–solid reactions: Theory, experiments and case studies relevant to earth and planetary

734 processes. *Reviews in Mineralogy and Geochemistry* 84, 1–56.
735 <https://doi.org/10.2138/rmg.2018.84.1>

736 Klose, K.B., Wood, J.A., Hashimoto, A., 1992. Mineral equilibria and the high radar reflectivity of Venus
737 mountaintops. *Journal of Geophysical Research: Planets* 97, 16353–16369.
738 <https://doi.org/10.1029/92JE01865>

739 Klose, K.B., Zolotov, M.Y., 1992. Chemical weathering of evolved igneous rocks on Venus, in: *Abstracts of*
740 *the Lunar and Planetary Science Conference*. Volume 23. p. 699.

741 Kohler, E., Chevrier, V.F., Gavin, P., Johnson, N., 2013. Experimental stability of tellurium and its
742 implications for the venusian radar anomalies. Presented at the 44th Lunar and Planetary
743 Science Conference. Abstract #2951.

744 Kohler, E., Chevrier, V.F., Johnson, N., Craig, P., Lacy, C., 2014. Proposed radar-reflective minerals tested
745 under Venus surface and atmospheric conditions. Presented at the 45th Lunar and Planetary
746 Science Conference. Abstract #2321.

747 Kohler, E., Gavin, P., Chevrier, V.F., Johnson, N., 2012. Experimental investigation into the radar
748 anomalies on the surface of Venus. Presented at the 43rd Lunar and Planetary Science
749 Conference. Abstract #2749.

750 Krasnopolsky, V.A., 2010. Spatially-resolved high-resolution spectroscopy of Venus 2. Variations of HDO,
751 OCS, and SO₂ at the cloud tops. *Icarus* 209, 314–322.
752 <https://doi.org/10.1016/j.icarus.2010.05.008>

753 Krasnopolsky, V.A., 2007. Chemical kinetic model for the lower atmosphere of Venus. *Icarus* 191, 25–37.
754 <https://doi.org/10.1016/j.icarus.2007.04.028>

755 Krasnopolsky, V.A., Parshev, V.A., 1981. Chemical composition of the atmosphere of Venus. *Nature* 292,
756 610–613. <https://doi.org/10.1038/292610a0>

757 Kumar, S., Taylor, H.A., 1985a. Deuterium on Venus: Model comparisons with pioneer Venus
758 observations of the predawn bulge ionosphere. *Icarus* 62, 494–504.
759 [https://doi.org/10.1016/0019-1035\(85\)90189-7](https://doi.org/10.1016/0019-1035(85)90189-7)

760 Kumar, S., Taylor, H.A., 1985b. Deuterium on Venus: Model comparisons with pioneer Venus
761 observations of the predawn bulge ionosphere. *Icarus* 62, 494–504.
762 [https://doi.org/10.1016/0019-1035\(85\)90189-7](https://doi.org/10.1016/0019-1035(85)90189-7)

763 Lazoryak, B.I., Morozov, V.A., Belik, A.A., Stefanovich, S.Yu., Grebenev, V.V., Leonidov, I.A., Mitberg, E.B.,
764 Davydov, S.A., Lebedev, O.I., Van Tendeloo, G., 2004. Ferroelectric phase transition in the
765 whitlockite-type Ca₉Fe(PO₄)₇; crystal structure of the paraelectric phase at 923 K. *Solid State*
766 *Sciences* 6, 185–195. <https://doi.org/10.1016/j.solidstatesciences.2003.12.007>

767 Lewis, J.S., 1970. Venus: Atmospheric and lithospheric composition. *Earth and Planetary Science Letters*
768 10, 73–80. [https://doi.org/10.1016/0012-821X\(70\)90066-X](https://doi.org/10.1016/0012-821X(70)90066-X)

769 Lewis, J.S., Kreimendahl, F.A., 1980. Oxidation state of the atmosphere and crust of Venus from pioneer
770 Venus results. *Icarus* 42, 330–337. [https://doi.org/10.1016/0019-1035\(80\)90098-6](https://doi.org/10.1016/0019-1035(80)90098-6)

771 Marcq, E., Mills, F.P., Parkinson, C.D., Vandaele, A.C., 2018. Composition and chemistry of the neutral
772 atmosphere of Venus. *Space Sci Rev* 214, 10. <https://doi.org/10.1007/s11214-017-0438-5>

773 Masursky, H., Eliason, E., Ford, P.G., McGill, G.E., Pettengill, G.H., Schaber, G.G., Schubert, G., 1980.
774 Pioneer Venus Radar results: Geology from images and altimetry. *Journal of Geophysical*
775 *Research: Space Physics* 85, 8232–8260. <https://doi.org/10.1029/JA085iA13p08232>

776 Mueller, N., Helbert, J., Hashimoto, G.L., Tsang, C.C.C., Erard, S., Piccioni, G., Drossart, P., 2008. Venus
777 surface thermal emission at 1 μm in VIRTIS imaging observations: Evidence for variation of crust
778 and mantle differentiation conditions. *Journal of Geophysical Research: Planets* 113.
779 <https://doi.org/10.1029/2008JE003118>

780 Mueller, R.F., 1964. A chemical model for the lower atmosphere of Venus. *Icarus* 3, 285–298.
781 [https://doi.org/10.1016/0019-1035\(64\)90037-5](https://doi.org/10.1016/0019-1035(64)90037-5)

782 Nozette, S., Lewis, J.S., 1982. Venus: Chemical weathering of igneous rocks and buffering of atmospheric
783 composition. *Science* 216, 181–183. <https://doi.org/10.1126/science.216.4542.181>

784 Palm, A.B., King, P.L., Renggli, C.J., Hervig, R.L., Dalby, K.N., Herring, A., Mernagh, T.P., Eggins, S.M.,
785 Troitzsch, U., Beeching, L., Kinsley, L., Guagliardo, P., 2018. Unravelling the consequences of
786 SO₂–basalt reactions for geochemical fractionation and mineral formation. *Reviews in*
787 *Mineralogy and Geochemistry* 84, 257–283. <https://doi.org/10.2138/rmg.2018.84.7>

788 Pettengill, G.H., Ford, P.G., Chapman, B.D., 1988. Venus: Surface electromagnetic properties. *Journal of*
789 *Geophysical Research: Solid Earth* 93, 14881–14892. <https://doi.org/10.1029/JB093iB12p14881>

790 Pettengill, G.H., Ford, P.G., Simpson, R.A., 1996. Electrical properties of the Venus surface from bistatic
791 radar observations. *Science* 272, 1628–1631. <https://doi.org/10.1126/science.272.5268.1628>

792 Pettengill, G.H., Ford, P.G., Wilt, R.J., 1992. Venus surface radiothermal emission as observed by
793 Magellan. *Journal of Geophysical Research: Planets* 97, 13091–13102.
794 <https://doi.org/10.1029/92JE01356>

795 Pieters, C.M., Head, J.W., Pratt, S., Patterson, W., Garvin, J., Barsukov, V.L., Basilevsky, A.T.,
796 Khodakovsky, I.L., Selivanov, A.S., Panfilov, A.S., Gektin, Y.M., Narayeva, Y.M., 1986. The color of
797 the surface of Venus. *Science* 234, 1379–1383. <https://doi.org/10.1126/science.234.4782.1379>

798 Port, S.T., Chevrier, V.F., Kohler, E., 2020. Investigation into the radar anomaly on Venus: The effect of
799 Venus conditions on bismuth, tellurium, and sulfur mixtures. *Icarus* 336, 113432.
800 <https://doi.org/10.1016/j.icarus.2019.113432>

801 Port, S.T., Kohler, E., Craig, P.I., Chevrier, V.F., 2016. Stability of pyrite under Venusian surface
802 conditions. Presented at the 47th Lunar and Planetary Science Conference. Abstract #2144.

803 Radoman-Shaw, B.G., Harvey, R.P., Costa, G.C.C., Jacobson, N.S., Avishai, A., Nakley, L.M., 2017. The
804 stability of calcium silicates and calcium carbonate on the surface of Venus. Presented at the
805 48th Lunar and Planetary Science Conference. Abstract #2701.

806 Renggli, C.J., King, P.L., 2018. SO₂ gas reactions with silicate glasses. *Reviews in Mineralogy and*
807 *Geochemistry* 84, 229–255. <https://doi.org/10.2138/rmg.2018.84.6>

808 Robie, R.A., Hemingway, B.S., 1995. Thermodynamic properties of minerals and related substances at
809 298.15 K and 1 bar (10⁵ pascals) pressure and at higher temperatures (USGS Numbered Series
810 No. 2131).

811 Salvador, A., Massol, H., Davaille, A., Marcq, E., Sarda, P., Chassefière, E., 2017. The relative influence of
812 H₂O and CO₂ on the primitive surface conditions and evolution of rocky planets. *Journal of*
813 *Geophysical Research: Planets* 122, 1458–1486. <https://doi.org/10.1002/2017JE005286>

814 Schaefer, L., Fegley, B., 2004. Heavy metal frost on Venus. *Icarus* 168, 215–219.
815 <https://doi.org/10.1016/j.icarus.2003.11.023>

816 Schmidt, M.E., Schrader, C.M., McCoy, T.J., 2013. The primary fO₂ of basalts examined by the Spirit
817 rover in Gusev Crater, Mars: Evidence for multiple redox states in the martian interior. *Earth and*
818 *Planetary Science Letters* 384, 198–208. <https://doi.org/10.1016/j.epsl.2013.10.005>

819 Seiff, A., Schofield, J.T., Kliore, A.J., Taylor, F.W., Limaye, S.S., Revercomb, H.E., Sromovsky, L.A.,
820 Kerzhanovich, V.V., Moroz, V.I., Marov, M.Ya., 1985. Models of the structure of the atmosphere
821 of Venus from the surface to 100 kilometers altitude. *Advances in Space Research* 5, 3–58.
822 [https://doi.org/10.1016/0273-1177\(85\)90197-8](https://doi.org/10.1016/0273-1177(85)90197-8)

823 Shellnutt, J.G., 2018. Derivation of intermediate to silicic magma from the basalt analyzed at the Vega 2
824 landing site, Venus. *PLOS ONE* 13, e0194155. <https://doi.org/10.1371/journal.pone.0194155>

825 Shellnutt, J.G., 2013. Petrological modeling of basaltic rocks from Venus: A case for the presence of
826 silicic rocks. *Journal of Geophysical Research: Planets* 118, 1350–1364.
827 <https://doi.org/10.1002/jgre.20094>

828 Simpson, R.A., Tyler, G.L., Häusler, B., Mattei, R., Pätzold, M., 2009. Venus Express bistatic radar: High-
829 elevation anomalous reflectivity. *Journal of Geophysical Research: Planets* 114.
830 <https://doi.org/10.1029/2008JE003156>

831 Skjelkvåle, B.-L., Amundsen, H.E.F., O'Reilly, S.Y., Griffin, W.L., Gjelsvik, T., 1989. A primitive alkali
832 basaltic stratovolcano and associated eruptive centres, Northwestern Spitsbergen: *Volcanology*
833 and tectonic significance. *Journal of Volcanology and Geothermal Research* 37, 1–19.
834 [https://doi.org/10.1016/0377-0273\(89\)90110-8](https://doi.org/10.1016/0377-0273(89)90110-8)

835 Surkov, Y.A., Barsukov, V.L., Moskalyeva, L.P., Kharyukova, V.P., Kemurdzhian, A.L., 1984. New data on
836 the composition, structure, and properties of Venus rock obtained by Venera 13 and Venera 14.
837 *Journal of Geophysical Research: Solid Earth* 89, B393–B402.
838 <https://doi.org/10.1029/JB089iS02p0B393>

839 Surkov, Y.A., Moskalyova, L.P., Kharyukova, V.P., Dudin, A.D., Smirnov, G.G., Zaitseva, S.Y., 1986. Venus
840 rock composition at the Vega 2 Landing Site. *Journal of Geophysical Research: Solid Earth* 91,
841 E215–E218. <https://doi.org/10.1029/JB091iB13p0E215>

842 Tanaka, K.L., Senske, D.A., Price, M., Kirk, R.L., 1997. Physiography, geologic/geomorphic mapping, and
843 stratigraphy of Venus, in: Bougher, S.W., Hunten, D.M., Phillips, R.J. (Eds.), *Venus II*. University of
844 Arizona Press, pp. 667–694.

845 Teffeteller, H., McCanta, M., Cherniak, D., Treiman, A.H., Filiberto, J., Rutherford, M.J., Johnson, N.,
846 2019. Experimental study of the alteration of basalt on the surface of Venus. Presented at the
847 50th Lunar and Planetary Science Conference. Abstract #1858.

848 Treiman, A.H., 2007. Geochemistry of Venus' surface: current limitations as future opportunities, in:
849 Esposito, L.W., Stofan, E.R., Cravens, T.E. (Eds.), *Exploring Venus as a Terrestrial Planet*,
850 *Geophysical Monograph Series* 176. American Geophysical Union, Washington, D. C., pp. 7–22.

851 Treiman, A.H., Harrington, E., Sharpton, V., 2016. Venus' radar-bright highlands: Different signatures and
852 materials on Ovda Regio and on Maxwell Montes. *Icarus* 280, 172–182.
853 <https://doi.org/10.1016/j.icarus.2016.07.001>

854 Treiman, A.H., Schwenzer, S.P., 2009. Basalt-atmosphere interaction on Venus: Preliminary results on
855 weathering of minerals and bulk rock. Presented at the Venus Geochemistry: Progress,
856 Prospects, and New Missions Workshop.

857 von Zahn, U., Kumar, S., Niemann, R., Prinn, R., 1983. Composition of the Venus atmosphere, in: Hunten,
858 D.M., Colin, L., Donahue, T.M., Moroz, V.I. (Eds.), *Venus*. University of Arizona Press, Tucson, p.
859 299.

860 Way, M.J., Genio, A.D.D., Kiang, N.Y., Sohl, L.E., Grinspoon, D.H., Aleinov, I., Kelley, M., Clune, T., 2016.
861 Was Venus the first habitable world of our solar system? *Geophysical Research Letters* 43,
862 8376–8383. <https://doi.org/10.1002/2016GL069790>

863 Weitz, C.M., Basilevsky, A.T., 1993. Magellan observations of the Venera and Vega landing site regions.
864 *Journal of Geophysical Research: Planets* 98, 17069–17097. <https://doi.org/10.1029/93JE01776>

865 Wood, J.A., 1997. Rock weathering on the surface of Venus, in: Bougher, S.W., Hunten, D.M., Phillips,
866 R.J. (Eds.), *Venus II: Geology, Geophysics, Atmosphere and Solar Wind Environment*. University
867 of Arizona Press, Tucson, pp. 637–664.

868 Yamanoi, Y., Nakashima, S., Katsura, M., 2009. Temperature dependence of reflectance spectra and
869 color values of hematite by in situ, high-temperature visible micro-spectroscopy. *American*
870 *Mineralogist* 94, 90–97. <https://doi.org/10.2138/am.2009.2779>

871 Zolotov, M., 2019. Chemical weathering on Venus. *Oxford Research Encyclopedia of Planetary Science*.
872 <https://doi.org/10.1093/acrefore/9780190647926.013.146>

873 Zolotov, M., 1996. A model for the thermal equilibrium of the surface venusian atmosphere. *GEOCHEM.*
874 *INT.* 33, 80–100.

875 Zolotov, M., Volkov, V.P., 1992. Chemical processes on the planetary surface. Venus geology,
876 geochemistry and geophysics 177–199.
877 Zolotov, M.Y., 1994. Phase relations in the Fe-Ti-Mg-O oxide system and hematite stability at the
878 condition of Venus' surface, in: 25th Lunar and Planetary Science Conference. Abstract #1571.
879 Zolotov, M.Y., Khodakovskiy, I.L., 1989. Exogenic processes, in: Barsukov, V.L., Volkov, V.P. (Eds.), The
880 Planet Venus: Atmosphere, Surface, Interior Structure. Nauka, Moscow, pp. 262–290.
881 Zolotov, M.Yu., 2018. Gas–solid interactions on Venus and other solar system bodies. Reviews in
882 Mineralogy and Geochemistry 84, 351–392. <https://doi.org/10.2138/rmg.2018.84.10>
883 Zolotov, M.Yu., 2015. 10.12 - Solid Planet–Atmosphere Interactions, in: Schubert, G. (Ed.), Treatise on
884 Geophysics (Second Edition). Elsevier, Oxford, pp. 411–427. <https://doi.org/10.1016/B978-0-444-53802-4.00182-2>
885
886 Zolotov, M.Yu., Fegley, B., Lodders, K., 1997. Hydrous silicates and water on Venus. Icarus 130, 475–494.
887 <https://doi.org/10.1006/icar.1997.5838>
888
889
890

891 **Table 1:** Solution models and pure phases used in phase equilibria calculations.

Mineral or solid solution, abbreviation used in Perple_X	Formula of main components	Abbreviation	Reference
Amphiboles			
Clinoamphibole, cAmph (G)	<i>tremolite:</i> $\text{Ca}_2\text{Mg}_5\text{Si}_8\text{O}_{22}(\text{OH})_2$	Amp	Green et al., 2016
	<i>Fe-tremolite:</i> $\text{Ca}_2\text{Fe}_5\text{Si}_8\text{O}_{22}(\text{OH})_2$		
	<i>grunerite:</i> $\text{Fe}_7\text{Si}_8\text{O}_{22}(\text{OH})_2$		
	<i>cummingtonite:</i> $\text{Mg}_7\text{Si}_8\text{O}_{22}(\text{OH})_2$		
	<i>pargasite:</i> $\text{Na}(\text{Ca},\text{Mg},\text{Fe})_2(\text{Mg},\text{Fe})_3(\text{Mg},\text{Fe})\text{AlSi}_6\text{Al}_2\text{O}_{22}(\text{OH})_2$		
	<i>K-pargasite</i> $\text{K}(\text{Ca},\text{Mg},\text{Fe})_2(\text{Mg},\text{Fe})_3(\text{Mg},\text{Fe})\text{AlSi}_6\text{Al}_2\text{O}_{22}(\text{OH})_2$		
	<i>tschermakite:</i> $(\text{Ca},\text{Mg},\text{Fe})_2(\text{Mg},\text{Fe})_3\text{Al}_2\text{Si}_6\text{Al}_2\text{O}_{22}(\text{OH})_2$		
	<i>Ti-Fe3+ tschermakite</i> $(\text{Ca},\text{Mg},\text{Fe})_2(\text{Mg},\text{Fe})_3(\text{Ti},\text{Fe}^{3+})_2\text{Si}_6\text{Al}_2\text{O}_{22}(\text{OH})_2$		
	<i>glaucophane-riebeckite:</i> $\text{Na}_2(\text{Mg},\text{Fe})_3(\text{Al},\text{Fe}^{3+})_2\text{Si}_8\text{O}_{22}(\text{OH})_2$		
	Pyroxenes		
Clinopyroxene, Augite(G)	<i>diopside:</i> $\text{CaMgSi}_2\text{O}_6$	Cpx	Green et al., 2016
	<i>hedenbergite:</i> $\text{CaFeSi}_2\text{O}_6$		
	<i>jadeite:</i>		

	$\text{NaAlSi}_2\text{O}_6$ <i>Ca-tschermaks:</i> $\text{CaAl}_2\text{SiO}_6$ <i>acmite:</i> $\text{NaFe}^{3+}\text{Si}_2\text{O}_6$		
Orthopyroxene, Opx(W)	<i>enstatite:</i> $\text{Mg}_2\text{Si}_2\text{O}_6$ <i>ferrosilite:</i> $\text{Fe}_2\text{Si}_2\text{O}_6$ <i>Mg-Fe-tschermaks:</i> $(\text{Mg,Fe})\text{Al}_2\text{SiO}_6$ <i>Fe³⁺-tschermaks:</i> $(\text{Mg,Fe})\text{Fe}^{3+}\text{AlSi}_2\text{O}_6$	Opx	White et al., 2014
Feldspars K-feldspar, Kf	<i>microcline:</i> KAlSi_3O_8 <i>albite:</i> $\text{NaAlSi}_3\text{O}_8$	Kfs	Thompson & Waldbaum, 1969
Plagioclase, Pl(h)	<i>high-albite:</i> $\text{NaAlSi}_3\text{O}_8$ <i>anorthite:</i> $\text{CaAl}_2\text{Si}_2\text{O}_8$	Pl	Newton et al., 1980
feldspar	<i>anorthite:</i> $\text{CaAl}_2\text{Si}_2\text{O}_8$ <i>microcline:</i> KAlSi_3O_8 <i>high-albite:</i> $\text{NaAlSi}_3\text{O}_8$	Fsp	Fuhrman and Lindsley, 1988
Phyllosilicates Chlorite, Chl(W)	<i>clinochlore:</i> $\text{Mg}_5\text{Al}_2\text{Si}_3\text{O}_{10}(\text{OH})_8$ <i>daphnite:</i> $\text{Fe}_5\text{Al}_2\text{Si}_3\text{O}_{10}(\text{OH})_8$ <i>amesite:</i> $\text{Mg}_4\text{Al}_4\text{Si}_2\text{O}_{10}(\text{OH})_8$ <i>Al-free-chlorite:</i> $\text{Mg}_6\text{Si}_4\text{O}_{10}(\text{OH})_8$	Chl	White et al., 2014
Biotite, Bio(TCC)	<i>annite:</i> $\text{KFe}_3\text{AlSi}_3\text{O}_{10}(\text{OH})_2$ <i>phlogopite:</i> $\text{KMg}_3\text{AlSi}_3\text{O}_{10}(\text{OH})_2$ <i>eastonite:</i> $\text{KMg}_2\text{Al}_3\text{Si}_2\text{O}_{10}(\text{OH})_2$ <i>ferric-biotite:</i> $\text{KMg}_2\text{Fe}^{3+}\text{Al}_2\text{Si}_2\text{O}_{10}(\text{OH})_2$ <i>titanium-biotite:</i> $\text{KMg}_2\text{TiAlSi}_3\text{O}_{10}(\text{O})_2$ <i>ordered biotite:</i> $\text{KMg}_2\text{FeAlSi}_3\text{O}_{10}(\text{OH})_2$	Bt	Tajčmanová et al., 2009

White mica, Mica (W)	<i>margarite:</i> $\text{CaAl}_4\text{Si}_2\text{O}_{10}(\text{OH})_2$ <i>muscovite:</i> $\text{KAl}_3\text{Si}_3\text{O}_{10}(\text{OH})_2$ <i>paragonite:</i> $\text{NaAl}_3\text{Si}_3\text{O}_{10}(\text{OH})_2$ <i>celadonite:</i> $\text{K}(\text{Fe},\text{Mg})\text{AlSi}_4\text{O}_{10}(\text{OH})_2$	Ms	White et al., 2014
Talc, T	<i>talc:</i> $\text{Mg}_3\text{Si}_4\text{O}_{10}(\text{OH})_2$ <i>Fe-talc:</i> $\text{Fe}_3\text{Si}_4\text{O}_{10}(\text{OH})_2$ <i>talc-tschemmaka:</i> $\text{Mg}_2\text{Al}_2\text{Si}_3\text{O}_{10}(\text{OH})_2$	Tlc	ideal
Other silicates			
Epidote, Ep (HP11)	<i>Fe-epidote:</i> $\text{Ca}_2\text{Fe}_2\text{AlSi}_3\text{O}_{12}(\text{OH})$ <i>clinozoisite:</i> $\text{Ca}_2\text{Al}_3\text{Si}_3\text{O}_{12}(\text{OH})$	Ep	Holland and Powell, 2011
Olivine, O(HP)	<i>forsterite:</i> Mg_2SiO_4 <i>fayalite:</i> Fe_2SiO_4	Oi	Holland and Powell, 1996; 1998
titanite (sphene)	CaTiSiO_5	ttn	pure
quartz	SiO_2	qz	pure
nepheline	$\text{NaAlSi}_3\text{O}_8$	nph	pure
leucite	KAlSi_2O_6	lct	pure
andalusite	Al_2SiO_5	and	pure
cordierite	$\text{Mg}_2\text{Al}_4\text{Si}_5\text{O}_{18}$	crd	pure
Carbonates			
Dolomite, Do(HP)	<i>dolomite</i> $\text{CaMg}(\text{CO}_3)_2$ <i>ankerite</i> $\text{CaFe}(\text{CO}_3)_2$	Dol	Holland and Powell, 1998
Magnesite, M(HP)	<i>magnesite</i> MgCO_3 <i>siderite</i> FeCO_3	Mgs	Holland and Powell, 1998
calcite	CaCO_3	pure	cal
Oxides			
Spinel, Sp(WPC)	<i>spinel:</i> MgAl_2O_4 <i>hercynite:</i> FeAl_2O_4	Spl	White et al., 2002

	<i>ulvöspinel:</i> Fe ₂ TiO ₄ <i>magnetite:</i> Fe ₃ O ₄		
Ilmenite, Ilm(WPH)	<i>ilmenite:</i> FeTiO ₃ <i>hematite</i> Fe ₂ O ₃ <i>geikielite:</i> MgTiO ₃	Ilm	White et al., 2000
hematite	Fe ₂ O ₃	hem	pure
magnetite	Fe ₃ O ₄	mag	pure
rutile	TiO ₂	rt	pure
Sulfides/sulfates			
pyrite	FeS ₂	py	pure
Pyrrhotite, Po(HP)	<i>troilite</i> FeS Fe _{0.88} S	Po	Holland and Powell, 1998
anhydrite	CaSO ₄	anh	pure

892

893

894

895 **Table 2:** Whole-rock starting compositions: basalt, alkali basalt, granite. Oxides are normalized

896 to 100 by Perple_X.

897

	Basalt ¹	Alkali Basalt ²	Granite ³
wt. %			
SiO ₂	48.7	47.9	71.4
TiO ₂	1.3	2.8	0.25
Al ₂ O ₃	17.9	18.00	12.38
FeO	8.8	9.6	4.59
MgO	8.1	3.3	0.16

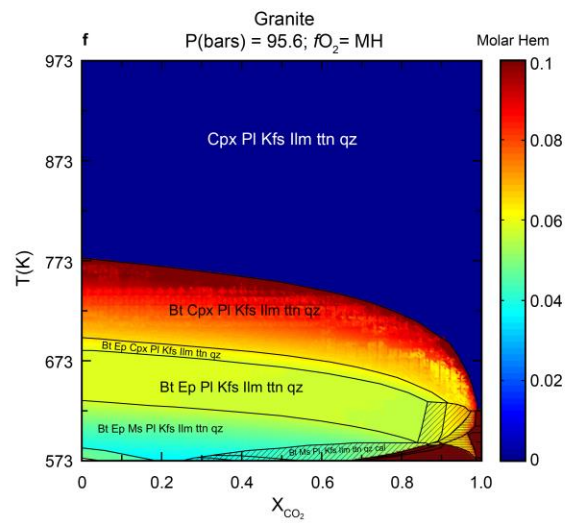
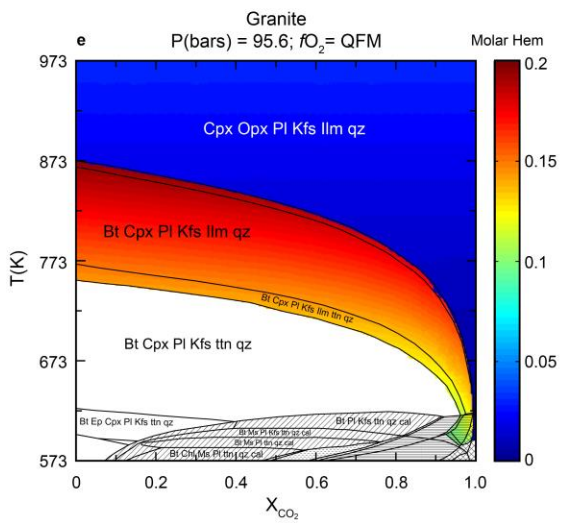
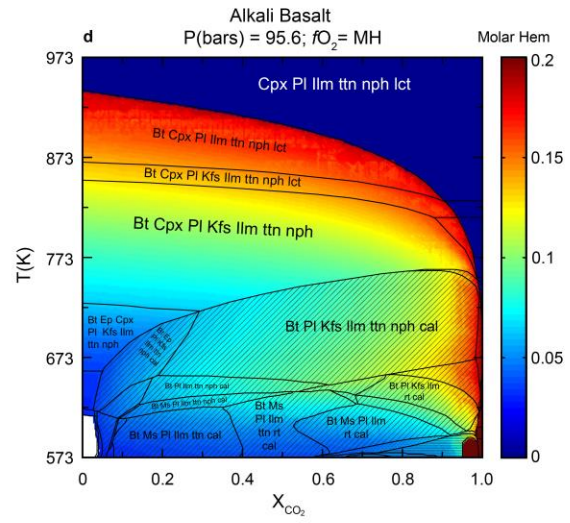
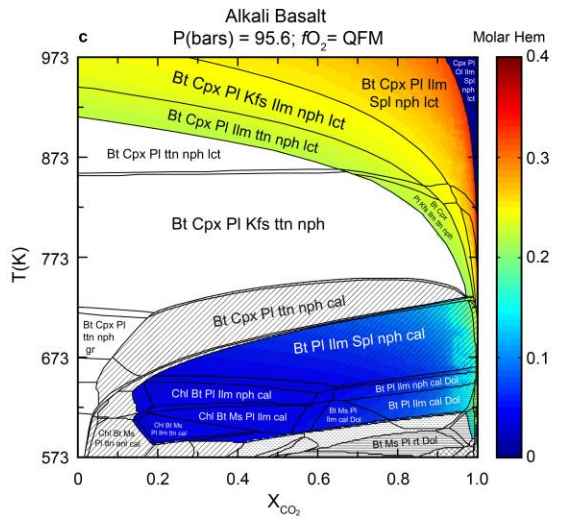
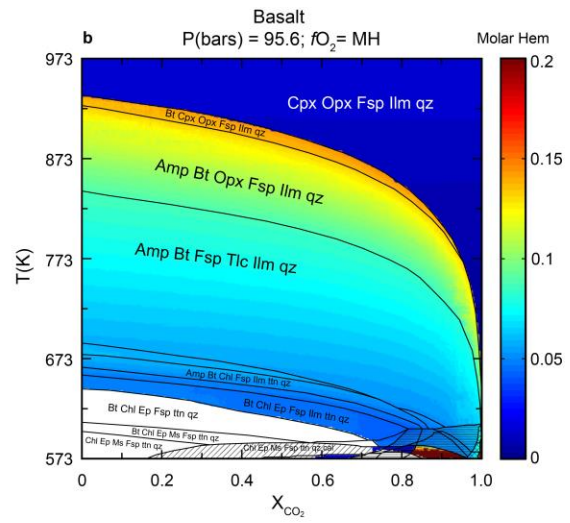
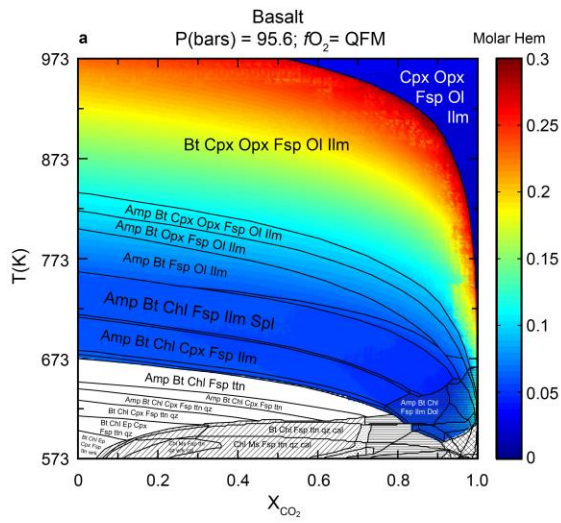
CaO	10.3	7.7	0.77
Na ₂ O	2.4	6.0	4.46
K ₂ O	0.2	2.7	4.28

References

¹ Treiman, 2007; Filiberto, 2014

² Skjelkvåle et al., 1989

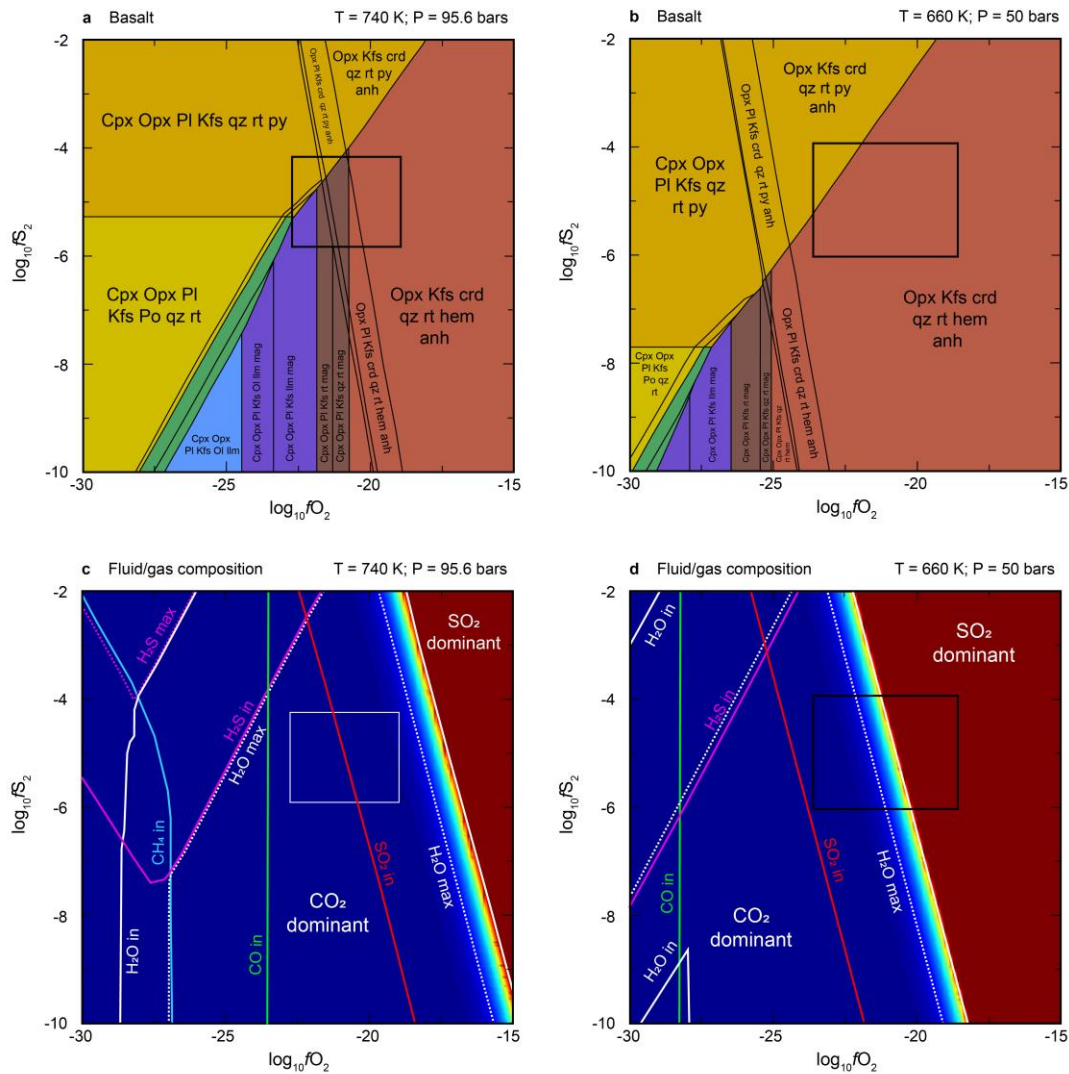
³ Auwera et al., 2003



900 **Figure 1:** Modeled mineral phases as a function of fluid composition (X_{CO_2}) and temperatures at
901 95.6 bars for the three protoliths (whole-rock compositions in Table 2) using the quartz-fayalite-
902 magnetite (QFM; a, c, e) and magnetite-hematite (MH; b, d, f) buffers. Color coding represents
903 the proportion of hematite in the hematite-ilmenite solid solution (abbreviated as Ilm), which varies
904 with protolith and oxygen buffers. Textures represent the following: calcite – diagonal lines; calcite
905 + dolomite – dashed lines; dolomite – solid lines; dolomite + magnesite – diamonds. Mineral
906 abbreviations are listed in Table 1.

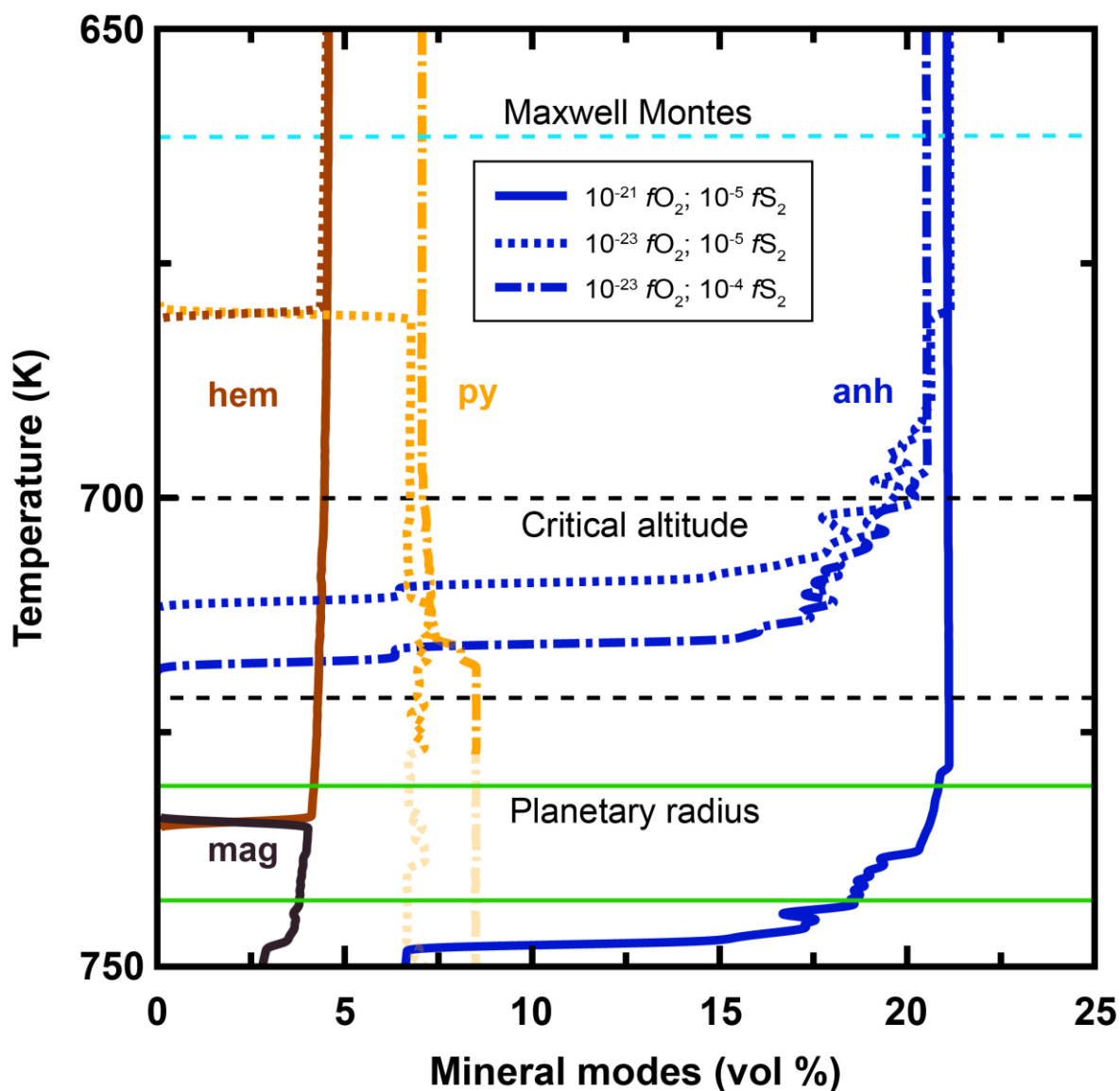
907

908



909

910 **Figure 2:** Phase equilibria for the basalt composition as a function of oxygen and sulfur fugacities
 911 and at temperature-pressure conditions relevant for planetary radius (740K, 95.6 bars; a) and
 912 high elevations (660 K, 50 bars; b). The black boxes represent fugacities that are most likely
 913 expected at planetary radius and at higher elevation, including larger uncertainties. Hematite –
 914 red, magnetite – brown, pyrite – dark yellow, pyrrhotite – bright yellow, ilmenite + magnetite –
 915 purple, ilmenite – blue, ilmenite + pyrrhotite – green. The composition of the gas in equilibrium
 916 with the solid phase is shown in c) and d). Solid lines represent the minimum amount of the
 917 species, while dashed lines represent the maximum amount. H₂ not shown due to limited stability.



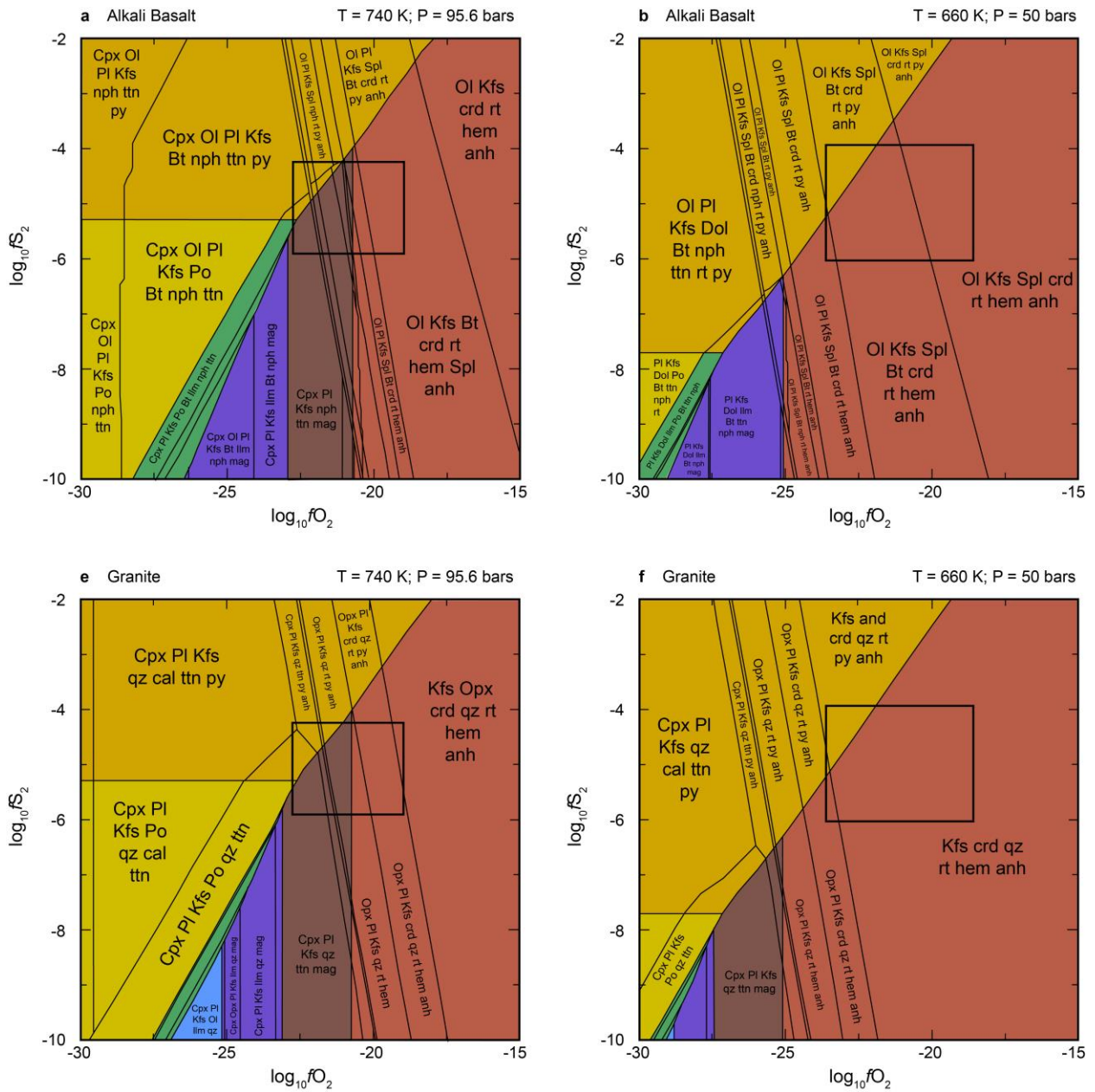
918

919 **Figure 3:** Modeled abundance of Fe-, and S-bearing minerals as a function of temperature at
 920 three different oxygen- and sulfur fugacities for the basaltic protolith. Temperature conditions at
 921 modal planetary radius are indicated by the green box. The critical altitude (dashed black box)
 922 represents altitudes at which the emissivity drops steeply and is estimated to lie between ~ 2 km
 923 up to 5 km depending on regional differences. The dashed cyan line represents conditions at the
 924 highest altitudes on Maxwell Montes. Solid lines: mineral modes calculated for conditions of fO_2
 925 = 10^{-21} and $fS_2 = 10^{-5}$ relevant for modal planetary radius. If these fugacities were constant with

926 decreasing temperature (and therefore altitude), pyrite would not be stable. Dashed lines: mineral
927 modes at lower oxygen fugacities than determined on Venus' surface with variations in sulfur
928 fugacities. If fugacities change with elevation, pyrite could be a stable phase at lower
929 temperatures and higher elevation. Pyrite is not expected to be stable at conditions relevant for
930 the modal planetary radius, which is indicated by the faded part of the curve.

931

932



933

934

935 **Supplementary Fig. 1:** Phase equilibria for the alkali basalt (a, b) and granite (c,d) compositions
 936 as a function of oxygen and sulfur fugacities and at temperature-pressure conditions relevant for
 937 planetary radius (740 K, 95.6 bar; a,c) and high elevations (660 K, 50 bar; b,d). The black boxes
 938 represent fugacities that are most likely expected at planetary radius and at higher elevation,

939 including larger uncertainties. Hematite – red, magnetite – brown, pyrite – dark yellow, pyrrhotite
940 – bright yellow, ilmenite + magnetite – purple, ilmenite – blue, ilmenite + pyrrhotite – green.